THE SEGUE STELLAR PARAMETER PIPELINE. IV. VALIDATION WITH AN EXTENDED SAMPLE OF GALACTIC GLOBULAR AND OPEN CLUSTERS

Jason P. Smolinski[1], Young Sun Lee[1], Timothy C. Beers[1], Deokkeun An[2], Steven J. Bickerton[3], Jennifer A. Johnson[4], Craig P. Loomis[3], Constance M. Rockosi[5], Thirupathi Sivarani[6], and Brian Yanny[7]

[1] Department of Physics and Astronomy and JINA (Joint Institute for Nuclear Astrophysics), Michigan State University, East Lansing, MI 48824, USA;
smolin19@msu.edu, lee@pa.msu.edu, beers@pa.msu.edu
[2] Department of Science Education, Ewha Womans University, Seoul 120-750, Republic of Korea; deokkeun@ewha.ac.kr
[3] Department of Astrophysical Sciences, Princeton University, Princeton, NJ 08544, USA; bick@astro.princeton.edu, cloomis@astro.princeton.edu
[4] Department of Astronomy, Ohio State University, 140 West 18th Avenue, Columbus, OH 43210, USA; jaj@astronomy.ohio-state.edu
[5] UCO/Lick Observatory, University of California, Santa Cruz, CA 95064, USA; crockosi@ucolick.org
[6] IIAP: Indian Institute of Astrophysics, II Block, Koramangala, Bangalore 560 034, India; sivarani@iiap.res.in
[7] Fermi National Accelerator Laboratory, P.O. Box 500, Batavia, IL 60510, USA; yanny@fnal.gov

ABSTRACT

Spectroscopic and photometric data for likely member stars of five Galactic globular clusters (M3, M53, M71, M92, and NGC 5053) and three open clusters (M35, NGC 2158, and NGC 6791) are processed by the current version of the SEGUE Stellar Parameter Pipeline (SSPP), in order to determine estimates of metallicities and radial velocities (RVs) for the clusters. These results are then compared to values from the literature. We find that the mean metallicity ($\langle[\text{Fe/H}]\rangle$) and mean radial velocity ($\langle\text{RV}\rangle$) estimates for each cluster are almost all within 2σ of the adopted literature values; most are within 1σ. We also demonstrate that the new version of the SSPP achieves small, but noteworthy, improvements in $\langle[\text{Fe/H}]\rangle$ estimates at the extrema of the cluster metallicity range, as compared to a previous version of the pipeline software. These results provide additional confidence in the application of the SSPP for studies of the abundances and kinematics of stellar populations in the Galaxy.

Key words: methods: data analysis – stars: abundances – stars: fundamental parameters – surveys – techniques: spectroscopic

Online-only material: color figures, machine-readable and VO tables

1. INTRODUCTION

The Sloan Digital Sky Survey (SDSS) and its extensions have now obtained *ugriz* photometry for several hundred million stars (through DR7; see Abazajian et al. 2009). The Sloan Extension for Galactic Understanding and Exploration (SEGUE; Yanny et al. 2009), one of the three sub-surveys that collectively formed SDSS-II, obtained *ugriz* imaging of some 3500 deg² of sky outside of the SDSS-I footprint (Fukugita et al. 1996; Gunn et al. 1998, 2006; Stoughton et al. 2002; Abazajian et al. 2003, 2004, 2005, 2009; Pier et al. 2003; Adelman-McCarthy et al. 2006, 2007, 2008), with special attention being given to scans of lower Galactic latitudes ($|b| < 35°$) in order to better probe the disk/halo interface of the Milky Way. SEGUE also obtained $R \simeq 2000$ spectroscopy over the wavelength range 3800–9200 Å for some 240,000 stars in 200 selected areas over the sky available from Apache Point, New Mexico. When combined with stars observed during SDSS-I, and the recently completed SEGUE-2 project within SDSS-III, a total of nearly 500,000 stars exploring the thin-disk, thick-disk, and halo populations of the Galaxy now have similar data.

The SEGUE Stellar Parameter Pipeline (SSPP; Lee et al. 2008a, 2008b; Allende Prieto et al. 2008) processes the wavelength- and flux-calibrated spectra generated by the standard SDSS spectroscopic reduction pipeline (Stoughton et al. 2002), obtains equivalent widths and/or line indices for 85 atomic or molecular absorption lines, and estimates T_{eff}, log g, and [Fe/H], along with radial velocities (RVs), through the application of a number of approaches (see Lee et al. 2008a, hereafter Paper I, for a detailed discussion of the techniques

employed by the SSPP; the Appendix of the present paper describes recent changes in the SSPP).

A previous validation paper by Lee et al. (2008b, hereafter Paper II) demonstrated, on the basis of comparisons with a sample of three Galactic globular clusters (GCs) and two open clusters (OCs), that the SSPP provides sufficiently accurate estimates of stellar parameters for use in the analysis of Galactic kinematics and chemistry, at least over the ranges in parameter space covered by these clusters (in particular, for the metallicity range $-2.4 < [\text{Fe/H}] < 0.0$). However, it was noted in that paper that the largest outliers in SSPP-derived metallicities were found for clusters near the extrema of this range. The team of researchers working on the SSPP has, in the time since publication of the original validation paper, endeavored to improve the performance of the SSPP near these extremes. As part of this effort, which is leading to the production of a version of the SSPP suitable for application to the DR8 release of results from SDSS-III (including the ~120,000 stars observed during SEGUE-2), we have assembled SDSS photometry and spectroscopy for an additional sample of five GCs (including two with [Fe/H] ~ −2.3: M92 and NGC 5053, and one intermediate-metallicity cluster with [Fe/H] ~ −0.7: M71), and three OCs, one of which has been shown in the literature to exhibit a super-solar metallicity, [Fe/H] = +0.3 (NGC 6791).

This paper, Paper IV in the series describing and testing the SSPP, examines the derived stellar parameters for our newly added clusters as well as for the previously reported sample of clusters, based on the most recent version of the SSPP. From this exercise, it is clear that the low-metallicity behavior of the SSPP has improved, and that the SSPP is also now

Table 1
Literature Properties of Globular and Open Clusters

Parameter	NGC 5053	M92 (NGC 6341)	M53 (NGC 5024)	M3 (NGC 5272)	M71 (NGC 6838)	NGC 2158	M35 (NGC 2168)	NGC 6791
R.A. (J2000)	13:16:27.0	17:17:07.3	13:12:55.2	13:42:11.2	19:53:46.1	06:07:25	06:08:54	19:20:53
Decl. (J2000)	+17:41:53	+43:08:11	+18:10:08.4	+28:22:32	+18:46:42	+24:05:48	+24:20:00	+37:46:18
(l, b)	(335.7, +78.9)	(68.3, +34.9)	(333.0, +79.8)	(42.2, +78.7)	(56.7, −4.6)	(186.6, +1.8)	(186.6, +2.2)	(70.0, +10.9)
[Fe/H]	−2.29[a]	−2.28[a]	−1.99[a]	−1.57[a]	−0.73[a]	−0.25[b]	−0.16[b]	+0.30[c]
[Fe/H]$_C$	−2.30	−2.35	−2.06	−1.50	−0.82	· · ·	· · ·	· · ·
$(m − M)_0$	16.12[d]	14.64[e]	16.25[a]	14.95[f]	12.86[f]	12.80[g]	9.80[h]	12.95[f]
$V_r\,(\mathrm{km\,s^{-1}})$	+44.0[a]	−120.3[a]	−79.1[a]	−147.6[a]	−22.8[a]	+28.0[b]	−8.2[b]	−57.0[b]
$E(B − V)$	0.017[e]	0.023[e]	0.021[e]	0.013[e]	0.275[i]	0.44[j]	0.20[h]	0.117[b]
r_t (arcmin)	13.67[a]	15.17[a]	21.75[a]	38.19[a]	8.96[a]	2.5[b]	20.0[b]	5.0[b]

Notes. Properties of the clusters in our sample as drawn from the literature, divided into globular clusters (left) and open clusters (right). The parameter r_t is the tidal radius in arc minutes for globular clusters or the apparent radius for open clusters. Exceptions to this are noted in Figure 1. The listed distance modulus $(m − M)_0$ is extinction corrected. The parameter [Fe/H]$_C$ is from the re-calibrated globular cluster metallicity scale of Carretta et al. (2009).
[a] Harris (1996).
[b] Dias et al. (2002).
[c] Boesgaard et al. (2009).
[d] Arellano Ferro et al. (2010).
[e] Schlegel et al. (1998).
[f] An et al. (2009).
[g] Carraro et al. (2002).
[h] Kalirai et al. (2003).
[i] Grundahl et al. (2002).
[j] Twarog et al. (1997).

capable of obtaining acceptable parameter estimates for stars up to solar metallicity, or slightly above. Section 2 describes the photometric and spectroscopic data for the eight clusters in our sample. The procedures for selecting likely true member stars in each cluster from among stars in the field are described in Section 3. Section 4 discusses the determination of $\langle$[Fe/H]$\rangle$ and $\langle$RV$\rangle$ estimates from the selected true member stars; these are compared to the values obtained by previous studies in Section 5. We then process the five clusters from Paper II through the current version of the SSPP and compare the results and improvements in Section 6. Section 7 provides a summary of our results. The Appendix describes the changes made in the SSPP since the previous version was released (and used for stellar parameter estimates in DR7). The present version of the SSPP should be very similar to that employed for the estimation of stellar parameters for stellar spectra in the next public release, DR8.

2. THE SAMPLE

We selected five Galactic GCs (M3, M53, M71, M92, and NGC 5053) and three OCs (M35, NGC 2158, and NGC 6791) which had already been observed by SDSS and processed by the SSPP. A number of other clusters were considered, but ultimately had to be rejected due to difficulties obtaining adequately reduced spectra from fields that were either too crowded or too heavily reddened. Because the default PHOTO pipeline (Lupton et al. 2001) was not designed to accurately deal with crowded fields such as those in the central regions of GCs, crowded-field photometric measurements were obtained using the DAOPHOT/ALLFRAME software package (Stetson 1987; Stetson 1994) for M3, M53, M71, M92, NGC 5053, and NGC 6791 (An et al. 2008). For the remaining clusters (M35 and NGC 2158) we followed the same procedures as in An et al. (2008) to obtain crowded-field photometry. Combining the SDSS photometry of the full field with the crowded-field photometry of the inner cluster regions, corrected for reddening

and extinction using values listed in Table 1, resulted in a nearly complete catalog of *ugriz* photometry for the stars in each cluster region. Table 1 summarizes the properties of each cluster included in this study. Metallicity values from the compilation of Harris (1996) are tabulated as well as values from the re-calibrated metallicity scale of Carretta et al. (2009).

The spectroscopic data were obtained during SEGUE observations using the ARC 2.5 m telescope, with stars targeted for spectroscopic follow-up selected from a photometric color–magnitude diagram (CMD) for each cluster. Stars located on the diagram in the regions of the main-sequence turnoff (MSTO) and red giant branch (RGB) were then selected as possible cluster members. Other stars in the field of each cluster were also selected by the default SEGUE target selection algorithm to fill each plug-plate, many of which ended up being cluster members themselves. Overall, SDSS spectroscopic data were obtained for 640 targets each in the regions of M3, M53, and NGC 5053, and 1280 targets each in the regions of M35, M71, M92, NGC 2158, and NGC 6791, including sky spectra and calibration objects. Some of these targets had low average signal-to-noise spectra; for consistency with previous papers in this series, only those spectra with $\langle$S/N$\rangle$ > 10/1 were considered for subsequent analysis. After processing by the SSPP some targets had no estimates for RV or [Fe/H]; these were excluded as well. After these cuts were made, there remained 487, 495, 579, 1094, 775, 495, 579, and 1087 stars considered for M3, M35, M53, M71, M92, NGC 2158, NGC 5053, and NGC 6791, respectively.

3. CLUSTER MEMBERSHIP SELECTION

Paper I has shown that the stellar spectra processed through the SSPP have typical uncertainties of 141 K, 0.23 dex, and 0.23 dex for T_{eff}, log g, and [Fe/H], respectively. Uncertainties in the RV depend on the spectral type and apparent magnitude (and fall in the range 5–20 km s^{-1}; for most of the cluster stars the error is usually much less than 10 km s^{-1}. In this
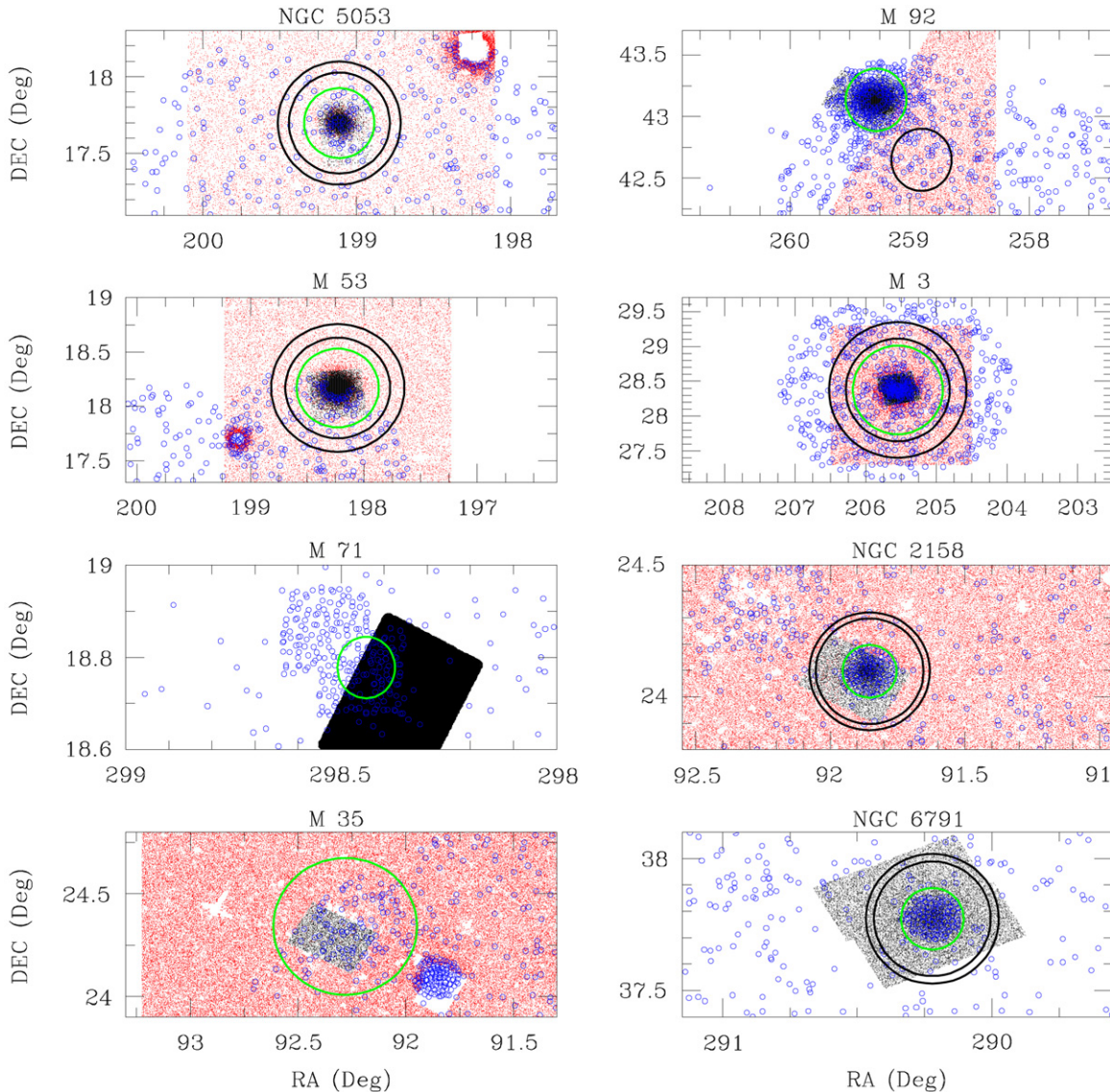
Figure 1. Stars with available photometry in the fields of NGC 5053, M92, M53, M3, M71, NGC 2158, M35, and NGC 6791. The black dots are stars from the crowded-field photometric analysis, the red dots are stars with photometry from the SDSS PHOTO pipeline, and the blue open circles are stars with SDSS spectroscopy. The green circle is the cluster's tidal radius (taken here as the cluster region) and the annulus between the two black circles constitutes the field region. The green circles are $13'.67$, $15'.17$, $21'.75$, $38'.19$, $4'.0$, $6'.0$, $20'.0$, and $7'.0$ in radius, respectively. In the case of M92, the cluster's proximity to the edge of the scan prevented an adequate annular field region; it was taken adjacent to the cluster region. NGC 2158 and NGC 6791 are open clusters, but due to their evolved nature, they are treated the same as globular clusters for the identification of likely true members. A larger radius was used for these clusters than those listed by Dias et al. (2002), in order to include as many member stars as possible.

section we discuss how the adopted true members for each cluster are selected, based in part on their estimated metallicities and RVs.

3.1. Likely Member Star Selection

The procedure for determining the likely members of each cluster is the same as described by Paper II, and will only be discussed briefly here. Two procedures were designed for selecting likely true member stars, one for GCs and one for OCs. The difference is primarily due to the lower number density of stars on the CMD of an open cluster compared to that of a GC. However, the techniques are sufficiently different that, due to the highly evolved nature of NGC 2158 and NGC 6791, the procedure for open clusters could not be applied to these particular clusters because it relies on a function fit to the main stellar locus which, in these cases, would be double-valued

around the MSTO. Hence, we have employed the procedure for GCs to the open clusters NGC 2158 and NGC 6791 and describe specific reasons for having done so where applicable.

Due to the limited number of stars with spectroscopic data, it was necessary to use the photometry to produce a well-defined CMD, over which the spectroscopic data were then plotted. The stars inside each cluster's tidal radius (r_t) were selected as the first cut of likely members, indicated by the green circles in Figure 1. Stars inside a concentric annulus (where possible) were selected as field stars indicated by the black circles in these figures. CMDs of both regions were obtained, then divided into sub-grids 0.2 mag wide in g_0 and 0.05 mag wide in $(g - r)_0$ color. Note that the field region of M92 (shown in Figure 1) is offset from the cluster center due to its position at the edge of the photometric scan. This was necessary because an annular field region around this location would have been inadequately populated with stars.

3
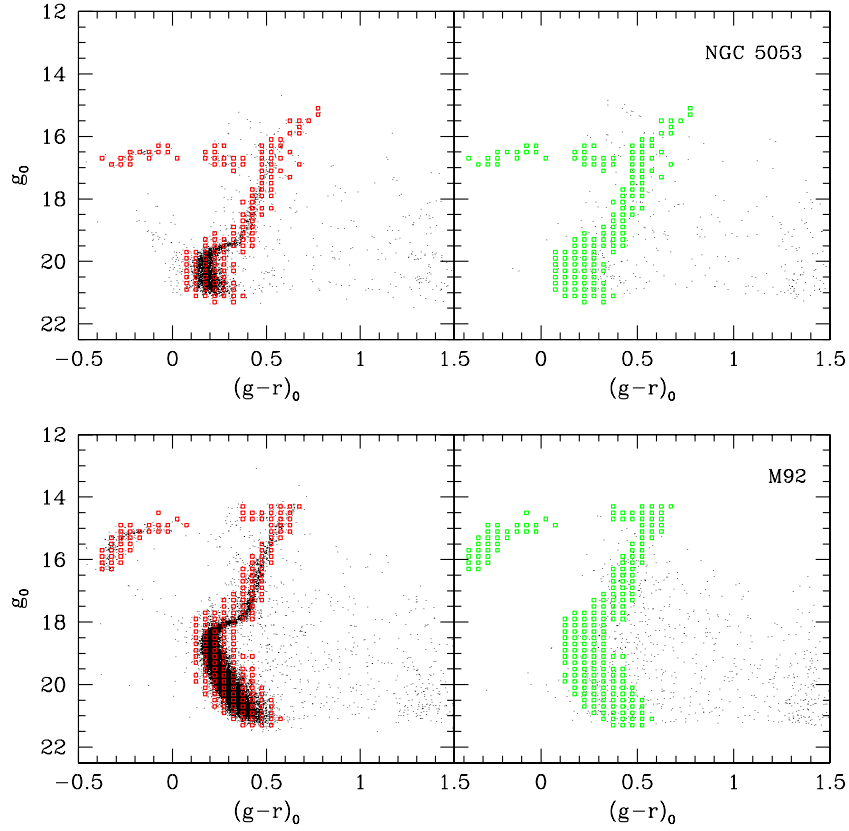
Figure 2. Color–magnitude diagrams of the stars from NGC 5053 (upper panels) and M92 (lower panels) inside the tidal radius (left-hand panels) and inside the field region (right-hand panels). The small boxes represent the sub-grids that were selected in the first cut of the CMD mask algorithm and contain the stars used the subsequent analysis.

(A color version of this figure is available in the online journal.)

In each sub-grid, the signal-to-noise (s/n) was calculated using

$$s/n(i, j) = \frac{n_c(i, j) - gn_f(i, j)}{\sqrt{n_c(i, j) + g^2 n_f(i, j)}}, \quad (1)$$

where n_c and n_f refer to the number of stars counted in each sub-grid with color index i and magnitude index j within the cluster region and field region, respectively, and the parameter g is the ratio of the cluster area to the field area. These values were sorted in descending order in an array with index l, then star counts were obtained in increasingly larger sections of the array. The area in each section is defined as $a_k = ka_l$, where $a_l = 0.01 \, \text{mag}^2$ represents the area of a single sub-grid and k is the number of sub-grids in the section. Then, the cumulative signal-to-noise ratio, S/N, as a function of a_k, was calculated using

$$S/N(a_k) = \frac{N_c(a_k) - gN_f(a_k)}{\sqrt{N_c(a_k) + g^2 N_f(a_k)}}, \quad (2)$$

where

$$N_c(a_k) = \sum_{l=1}^{k} n_c(l), \qquad N_f(a_k) = \sum_{l=1}^{k} n_f(l). \quad (3)$$

Here, $n_c(l)$ represents the number of cluster stars within the ordered sub-grid array element l and $n_f(l)$ represents the same quantity for the field stars. A threshold value for s/n was adopted, based on the maximum value of $S/N(a_k)$, to identify areas of the CMD where the ratio of cluster stars to field stars was high (rejecting single-star events). These areas were taken

to be sub-grids of likely cluster members and all sub-grids with s/n(i, j) greater than this threshold were identified. These sub-grids are shown as boxes in Figures 2–4. The left-hand panels show the stars inside the tidal radius—the sub-grids with s/n greater than the threshold value are indicated as red squares. The right-hand panels show the stars from the field region with the same sub-grids indicated in green.

The procedures described in Paper II handle OCs differently from GCs, primarily due to the fact that no field region is required. Instead of determining sub-grid s/n ratios, a fiducial line is fit to the OC's main sequence (MS) using a polynomial fitting routine, then a region is picked out by eye corresponding to the MS to represent the likely member stars. The interested reader is referred to Paper II for further details on the OC member selection procedure. This procedure works well on young clusters, where no significant evolution off the MS has occurred. However, NGC 2158 and NGC 6791 are evolved (older) clusters and exhibit a distinct MSTO and RGB (see Figure 4). This prevents polynomial fitting of the CMD from working properly since the function would be double valued, so in this study NGC 2158 and NGC 6791 are processed (for the purpose of member assignment) as if they are GCs. The usual OC procedure was successfully implemented for M35 (Figure 5).

The cleaned CMDs for our sample are shown in Figures 6 and 7. The black points are the likely members from the photometry, while the red open circles are the likely members from the spectroscopic sample. This part of the procedure could not be carried out for M71 due to difficulties encountered with the photometry values available for this cluster at the time of our
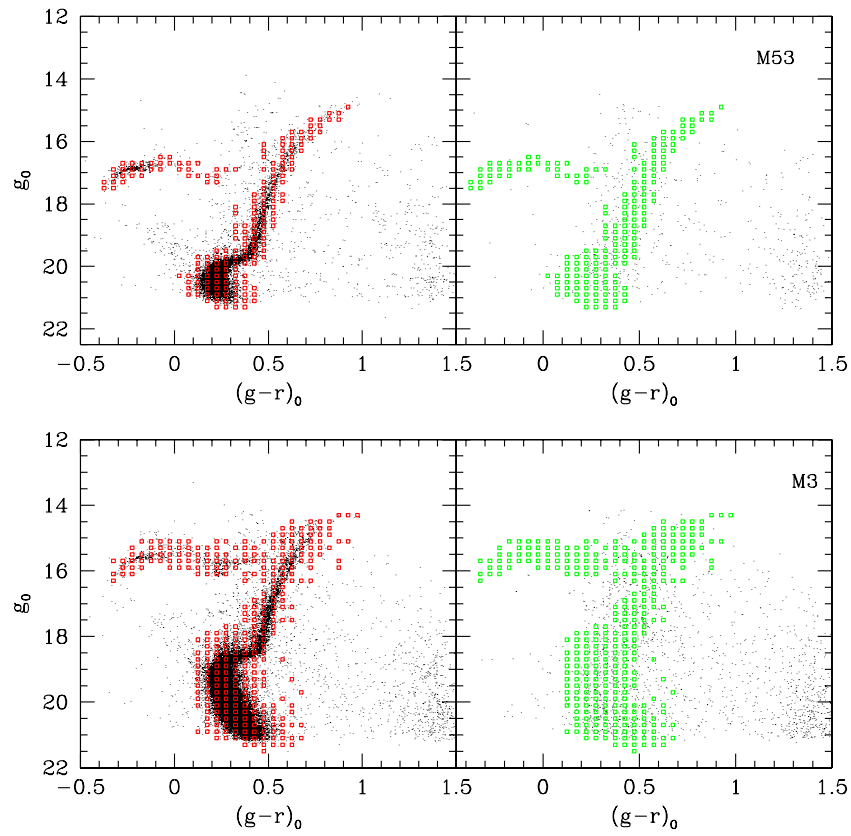
Figure 3. Same as Figure 2, but for M53 (upper panels) and M3 (lower panels).
(A color version of this figure is available in the online journal.)
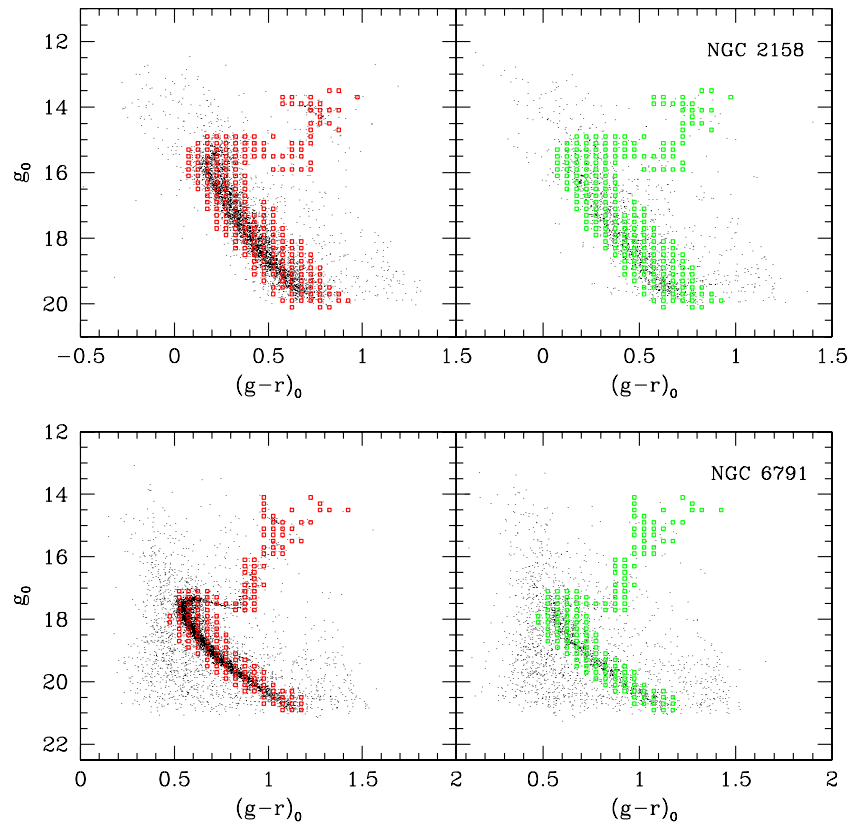
Figure 4. Same as Figure 2, but for NGC 2158 (upper panels) and NGC 6791 (lower panels). Due to the highly evolved nature of these open clusters, they were treated in the member selection process as if they were globular clusters.

(A color version of this figure is available in the online journal.)

5
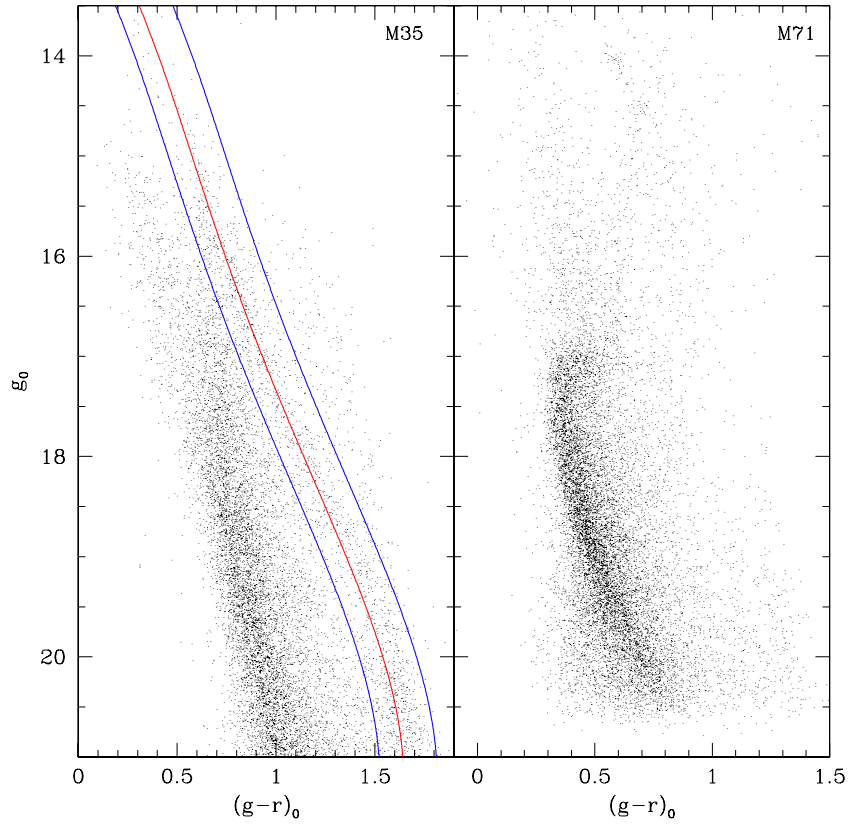
Figure 5. Same as Figure 2, but for M35 (left-hand panel) and M71 (right-hand panel). The red line in M35 is the fiducial from a fourth-order polynomial fit, while the blue lines define the offsets of $^{+0.17}_{-0.12}$ mag inside of which were selected stars regarded as likely members from the photometric data. Because of M35's low Galactic latitude, the dense stripe of stars on the blue side of the main sequence is due to superposed disk stars. Member stars for M71 were selected strictly by radial velocity and metallicity cuts rather than by using the CMD first; no photometry was used for analysis of this cluster due to poor calibration. For this reason, the CMD for M71 is shown differently from the other globular clusters.

(A color version of this figure is available in the online journal.)

analysis (see An et al. 2008). Therefore, a first cut was made based on the tidal radius of the stars, and those stars were passed on to the final step, as outlined in the following section. Figure 5 shows the first-cut CMD for M71.

3.2. Selection of Adopted True Members

We next determine the true member stars as a subset of the adopted likely member stars. Figure 8 shows the distributions of [Fe/H] (left-hand panel) and RVs (RVs; right-hand panel) for stars in the field of NGC 5053 at each culling point in the procedure. The black lines indicate all 579 stars on the original spectroscopic plate (after removing stars with no parameter estimates from the SSPP or low spectral S/N), while the red lines indicate only those stars inside r_t and the green lines indicate those stars that passed the cut using the individual sub-grid s/n and cumulative S/N calculations. We then performed a Gaussian fit to the highest peak of the distribution of this final subset (blue line) and obtained estimates of the mean and standard deviation of [Fe/H] and RV. Finally, outliers were rejected by applying a 2σ cut on both parameters:

$$\langle [\text{Fe/H}] \rangle - 2\sigma_{[\text{Fe/H}]} \leqslant [\text{Fe/H}]_\star \leqslant \langle [\text{Fe/H}] \rangle + 2\sigma_{[\text{Fe/H}]} \quad (4)$$

$$\langle \text{RV} \rangle - 2\sigma_{\text{RV}} \leqslant \text{RV}_\star \leqslant \langle \text{RV} \rangle + 2\sigma_{\text{RV}}. \quad (5)$$

$[\text{Fe/H}]_\star$ and $\text{RV}_\star$ correspond to the metallicity and RV of each star in question. If a star passed both cuts then it was considered a true member star. The numbers of true member stars determined by this final cut for each cluster are listed in Table 2.

4. DETERMINATION OF OVERALL METALLICITIES AND RADIAL VELOCITIES OF THE CLUSTERS

Once the true members were selected as described above, final estimates of the cluster metallicities and RVs were obtained. Figures 8–15 show binned distributions of [Fe/H] and RV for each cluster. The black lines in these figures represent the full distribution of all stars in each cluster's field with available spectroscopic information, the red lines represent only those stars from the spectroscopic samples that lie inside each cluster's tidal radius (or a reasonable radius, for M71 and NGC 6791), and the green lines represent those stars that passed the sub-grid s/n cut described in Section 3.1. Gaussian fits (blue lines) to the highest peak of this final distribution determined the adopted cluster values, which are listed in Table 2. This table also lists the standard error in the mean (σ_μ) for the estimates of metallicity and RV for each cluster; due to the large numbers of true members for each cluster, these are uniformly small.

No strong trends appear to exist in estimates of [Fe/H] as a function of color or spectral quality, as shown in Figures 16 and 17. As a check, we calculated residuals of [Fe/H] with respect to the values adopted for each cluster from the literature, using

$$\text{Res}_{[\text{Fe/H}]} = [\text{Fe/H}] - [\text{Fe/H}]_{\text{lit}}, \quad (6)$$

and performed a linear regression on these values as a function of $(g - r)_0$ color and $\langle \text{S/N} \rangle$ using models of the form

$$\text{Res}_{[\text{Fe/H}]} = X \cdot (g - r)_0 + Y \quad (7)$$
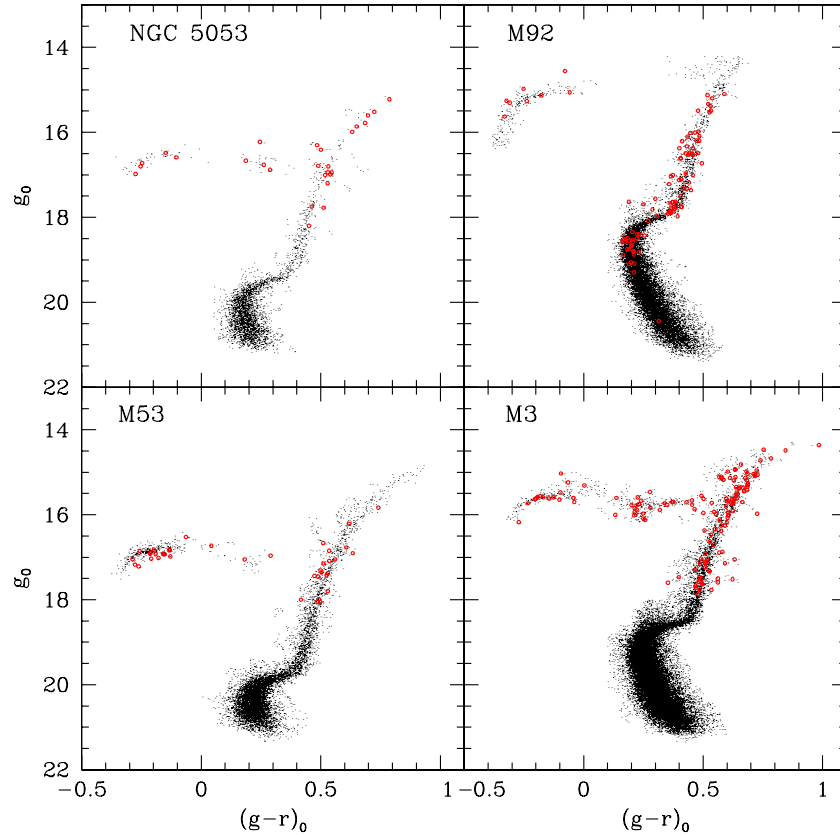
Figure 6. Color–magnitude diagram following the second cut of likely member stars based on the sub-grid selection for NGC 5053 (upper-left panel), M92 (upper-right panel), M53 (lower-left panel), and M3 (lower-right panel). Black dots represent stars from the photometric sample and the red open circles represent stars from the spectroscopic sample.

(A color version of this figure is available in the online journal.)

Table 2
Measured Metallicities and Radial Velocities of Globular and Open Clusters

Cluster	$\langle$[Fe/H]$\rangle$	σ([Fe/H]) (dex)	σ_μ([Fe/H]) (dex)	$\langle$RV$\rangle$ (km s^{-1})	σ(RV) (km s^{-1})	σ_μ(RV) (km s^{-1})	N
NGC 5053	−2.26	0.25	0.06	+44.0	4.9	1.2	16
M92	−2.25	0.17	0.02	−116.5	8.7	1.1	58
M53	−2.03	0.13	0.03	−59.6	7.9	1.8	19
M3	−1.55	0.14	0.02	−141.2	5.6	0.6	77
M71	−0.79	0.06	0.01	−16.9	9.3	2.3	17
NGC 2158	−0.26	0.08	0.01	+27.8	5.9	0.7	62
M35	−0.20	0.18	0.03	−5.0	6.2	1.2	29
NGC 6791	+0.31	0.13	0.01	−47.0	6.0	0.6	90

Notes. Columns 2 and 5 list the measured mean values of [Fe/H] and RV for each cluster, while Columns 3 and 6 list the 1σ spread of each value. Columns 4 and 7 are the standard errors in the mean (σ_μ) of the estimates. N lists the number of true member stars for each cluster determined by the final application of the 2σ range to the mean of the Gaussian fits on [Fe/H] and RV.

$$\mathrm{Res}_{[Fe/H]} = X \cdot (S/N) + Y. \qquad (8)$$

The results of the linear regressions are listed in Table 3. Column 2 lists the number of true member stars used in the fit, Columns 4 and 6 list the slope and zero point of the fit, respectively, while Columns 5 and 7 list the corresponding uncertainties. Finally, Column 8 lists the R^2 value, which indicates the amount of scatter in the data that can be accommodated by the regression. Values of R^2 close to zero indicate little dependence on the independent variable (the desired goal), whereas values of R^2 close to one indicate a large dependence on the

independent variable. There are two clusters (NGC 5053 and M35) for which the R^2 values are somewhat high. These appear to have been influenced by stars at the extrema of the color ranges, but still do not rise to the level of strong statistical significance. The fits for the rest of the clusters have sufficiently low values of R^2 that the correlations are not statistically significant; Figures 18 and 19 show the distribution of metallicity estimates as a function of the estimated surface gravity. No significant trends are observed, supporting the conclusion of Paper II that the SSPP is robust and reliable over large ranges in surface gravity (luminosity) and color, even for spectra with less-than-optimal S/N.
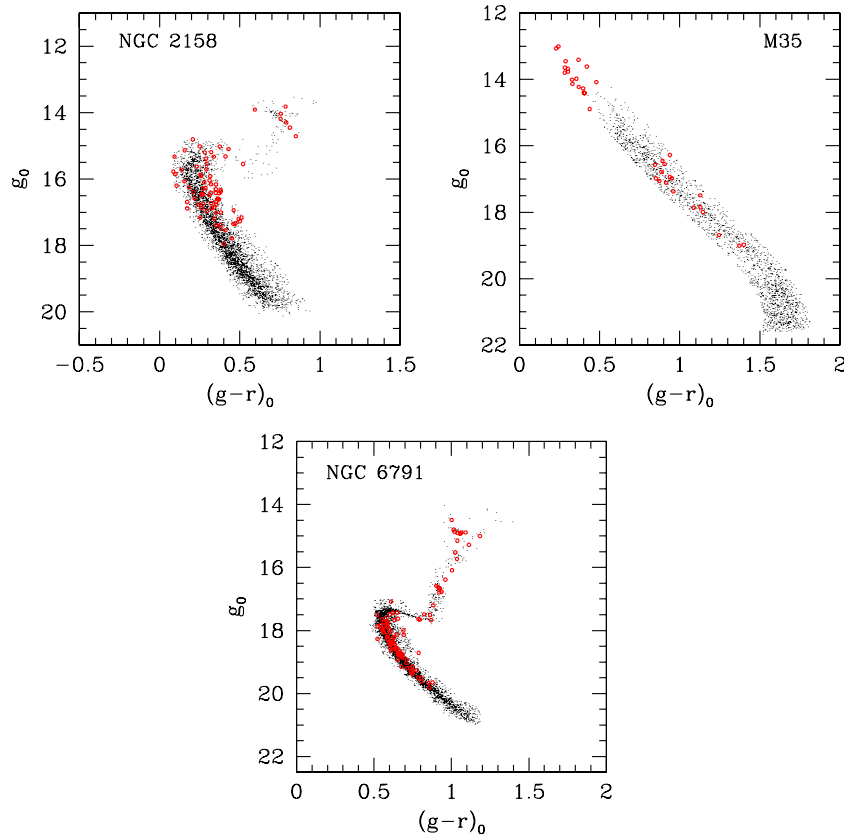
Figure 7. Color–magnitude diagram following the second cut of likely member stars for NGC 2158 (upper-left panel), M35 (upper-right panel), and NGC 6791 (lower panel). Black dots represent stars from the photometric sample and the red open circles represent stars from the spectroscopic sample.

(A color version of this figure is available in the online journal.)

Table 3
Linear Regression on [Fe/H] Residuals

Cluster (1)	N (2)	Parameter (3)	X (4)	σ_X (5)	Y (6)	σ_Y (7)	R^2 (8)
NGC 5053	16	$(g-r)_0$	−0.585	0.164	+0.347	0.090	0.475
		S/N	−0.007	0.005	+0.333	0.182	0.133
M92	58	$(g-r)_0$	−0.347	0.145	+0.229	0.053	0.093
		S/N	−0.001	0.002	+0.135	0.051	0.004
M53	19	$(g-r)_0$	+0.166	0.138	+0.027	0.066	0.078
		S/N	−0.005	0.006	+0.192	0.132	0.048
M3	77	$(g-r)_0$	−0.219	0.056	+0.059	0.032	0.071
		S/N	+0.001	0.001	−0.085	0.044	0.022
M71	17	$(g-r)_0$	+0.017	0.177	+0.089	0.116	0.001
		S/N	−0.001	0.001	+0.140	0.078	0.018
NGC 2158	62	$(g-r)_0$	+0.017	0.047	−0.008	0.019	0.002
		S/N	+0.002	0.001	−0.099	0.036	0.110
M35	29	$(g-r)_0$	−0.289	0.062	+0.121	0.044	0.445
		S/N	+0.006	0.001	−0.451	0.084	0.468
NGC 6791	90	$(g-r)_0$	+0.276	0.077	−0.191	0.058	0.128
		S/N	+0.003	0.001	−0.110	0.040	0.103

Notes. The variables X and Y are the slope and zero points, respectively, of a linear regression on the residuals in our measured [Fe/H] values and those adopted from the literature, along with the corresponding uncertainties from the regression. The parameter R^2 indicates the fraction of the variance accounted for by the correlations in the variables $(g-r)_0$ and S/N for each cluster.

The SSPP-estimated temperatures and surface gravities for true member stars are plotted in Figures 20–27 over the cleaned CMDs of the likely member stars from the photometric sample that passed the s/n cut. The spectroscopic data points are plotted in different colors, in temperature steps of 500 K and log g steps of 0.5 dex. Stars at the top of the MS and on the MSTO have generally lower S/N than those on the RGB and horizontal branch (HB), so the fact that some non-uniformity is observed in the distribution of $T_{\rm eff}$ and log g in stars near the MSTO is not unexpected.

Table 4 lists the SSPP-derived properties for all stars selected as true cluster members from each cluster, as well as the
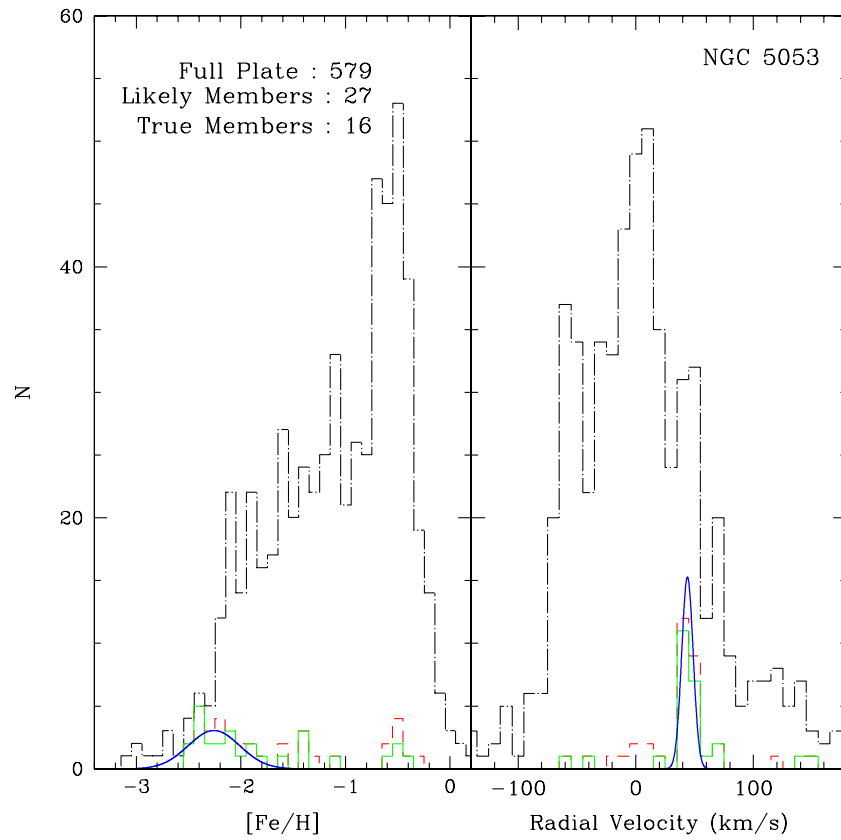
Figure 8. Distributions of [Fe/H] and radial velocity for stars in the field of NGC 5053. The black dot-dashed line corresponds to all the stars on the plate, the red dashed line corresponds to the stars inside the tidal radius, and the green solid line corresponds to the stars that were identified as likely members by the sub-grid s/n procedure described in Section 3.1. The blue solid line is a Gaussian fit indicating the region of each distribution in which the true members are located, as described in Section 3.2.

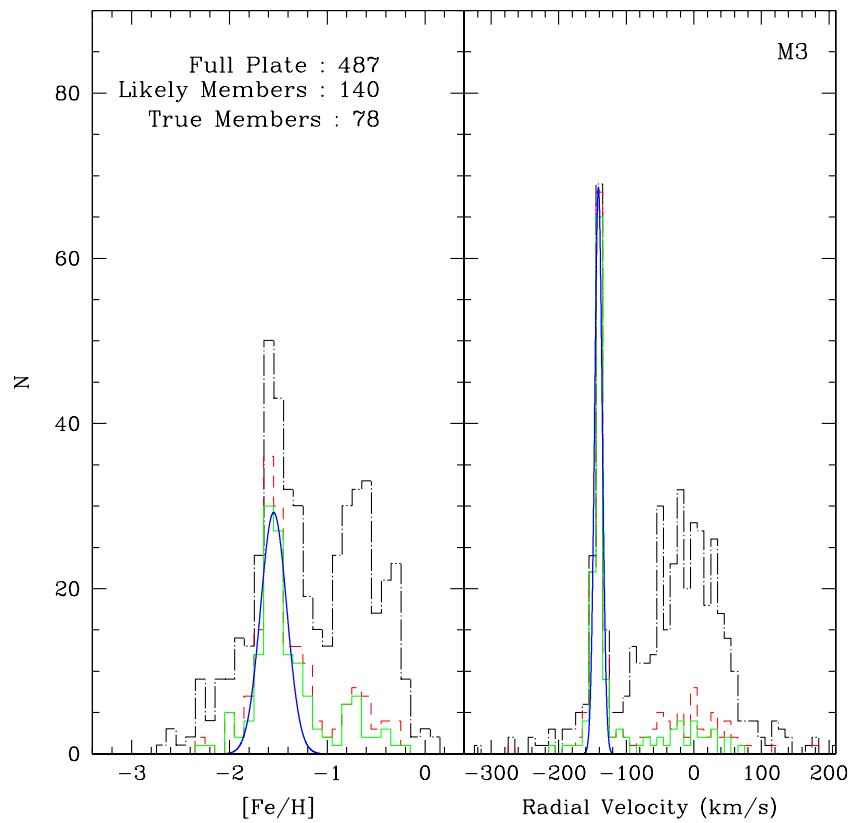(A color version of this figure is available in the online journal.)
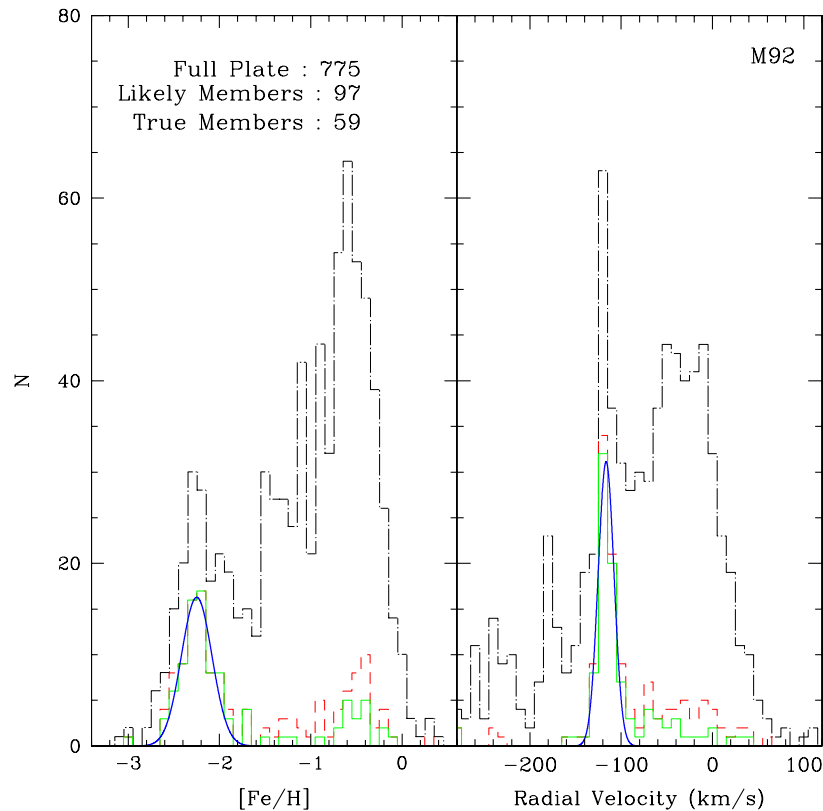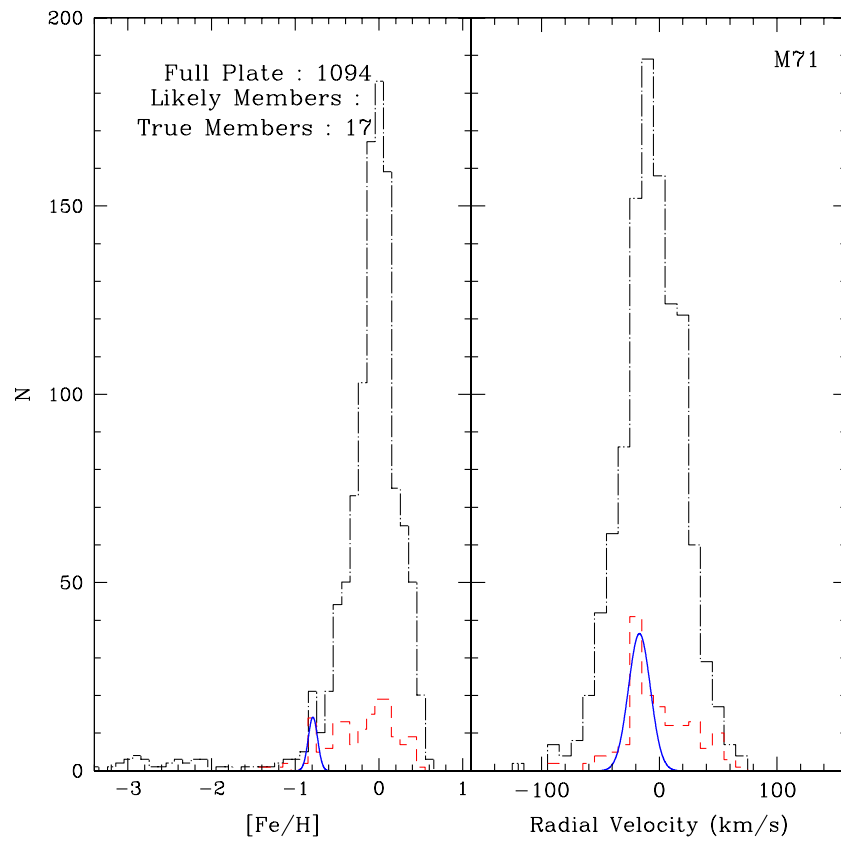

Figure 9. Same as Figure 8, but for M92.

(A color version of this figure is available in the online journal.)

9
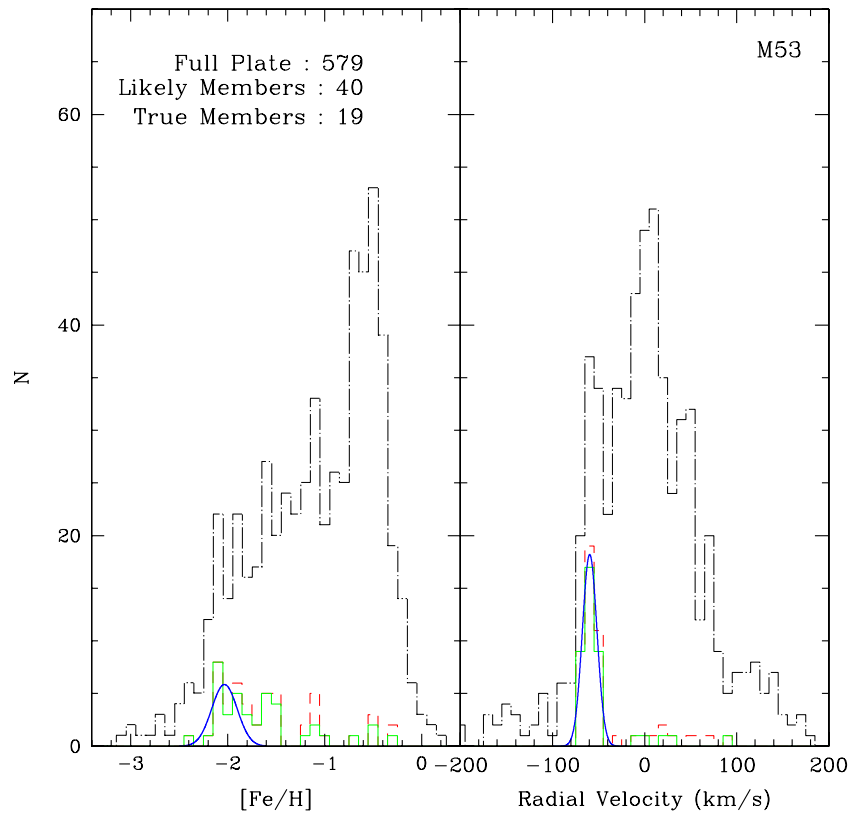
Figure 10. Same as Figure 8, but for M53.

(A color version of this figure is available in the online journal.)

Figure 11. Same as Figure 8, but for M3.

(A color version of this figure is available in the online journal.)

Figure 12. Same as Figure 8, but for M71.

(A color version of this figure is available in the online journal.)

Figure 13. Same as Figure 8, but for NGC 2158.

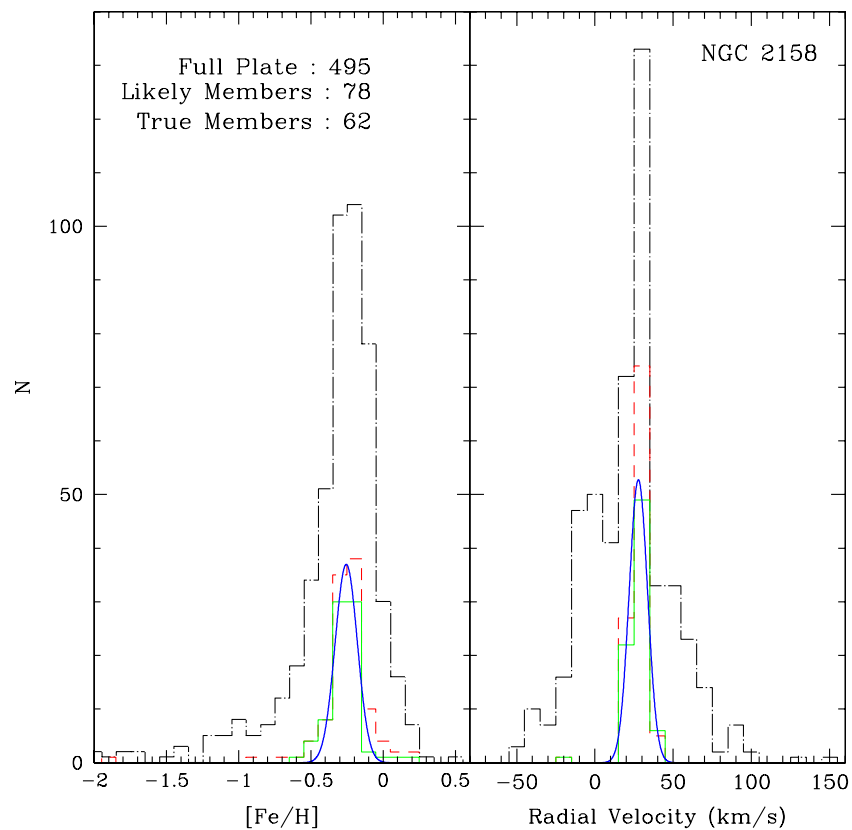(A color version of this figure is available in the online journal.)
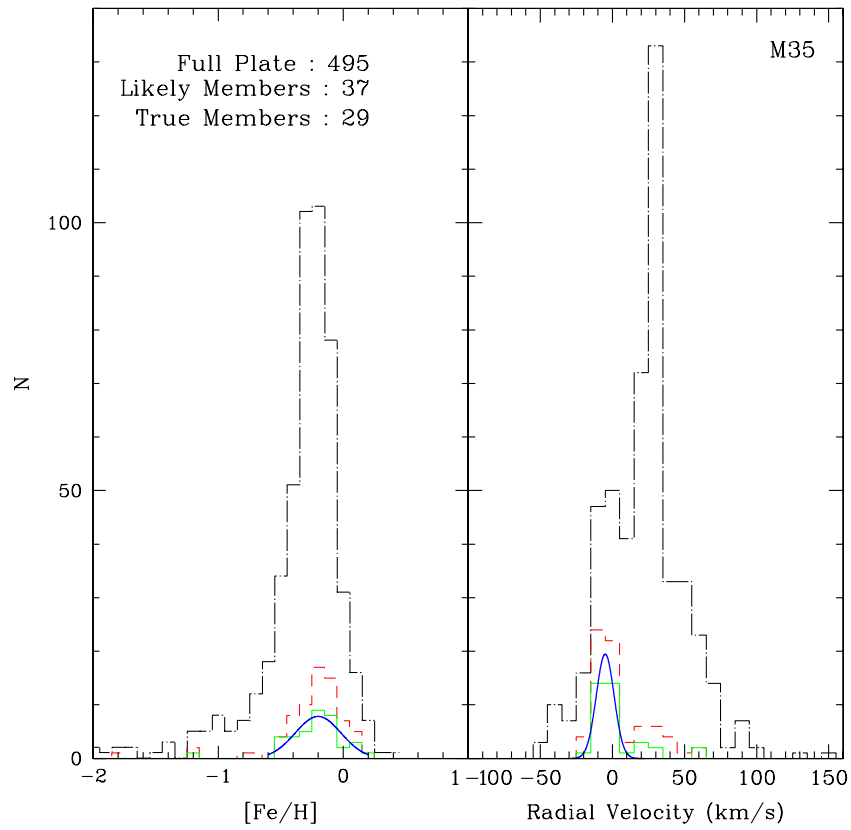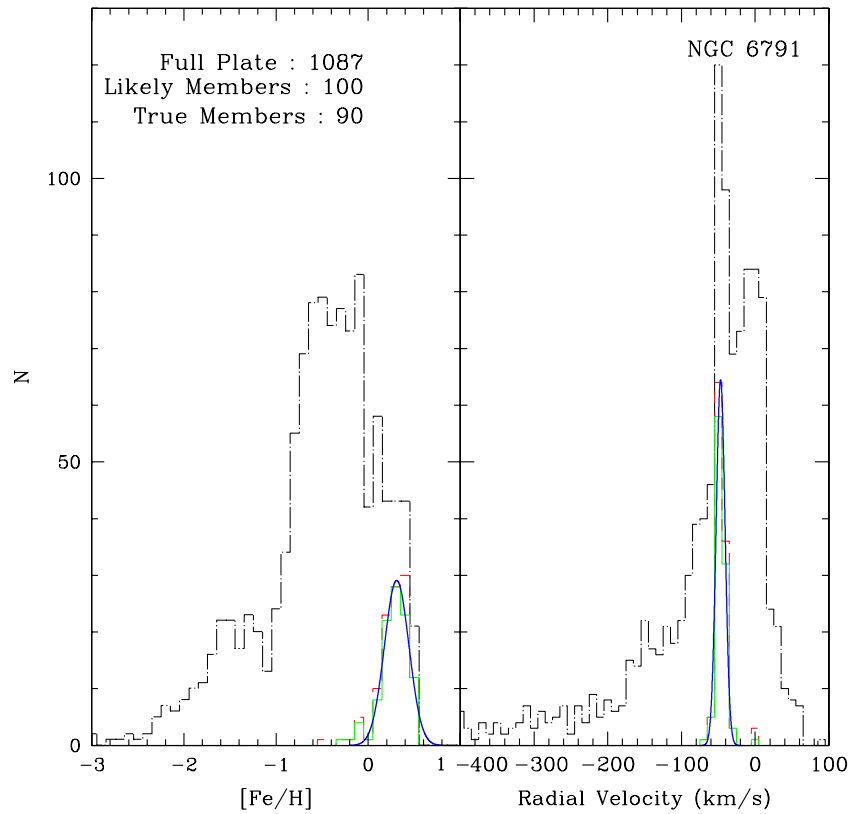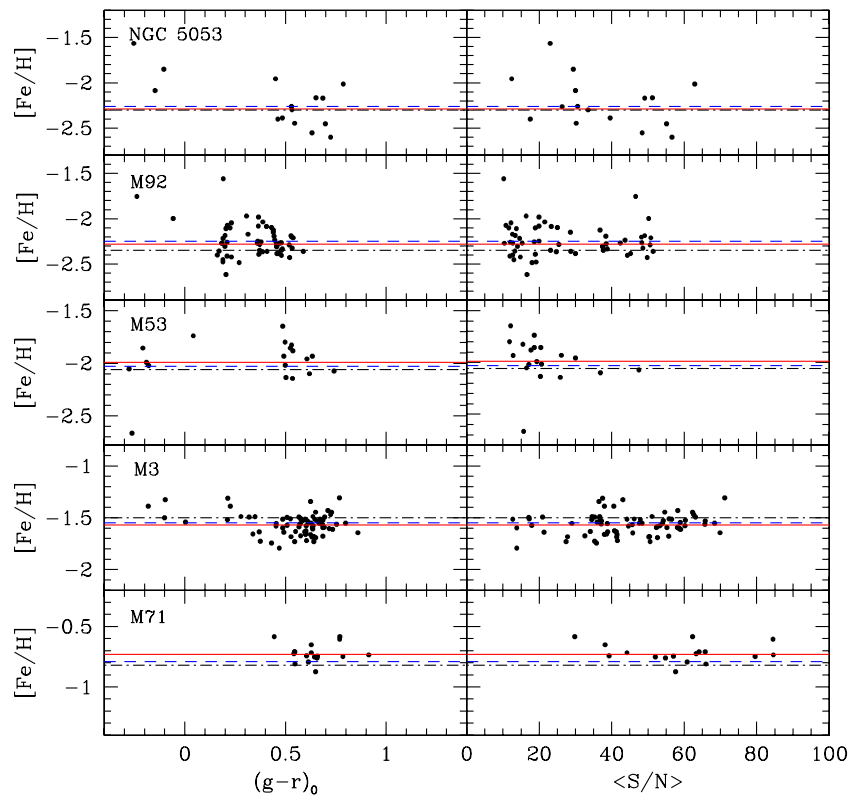
11

Figure 14. Same as Figure 8, but for M35.

(A color version of this figure is available in the online journal.)
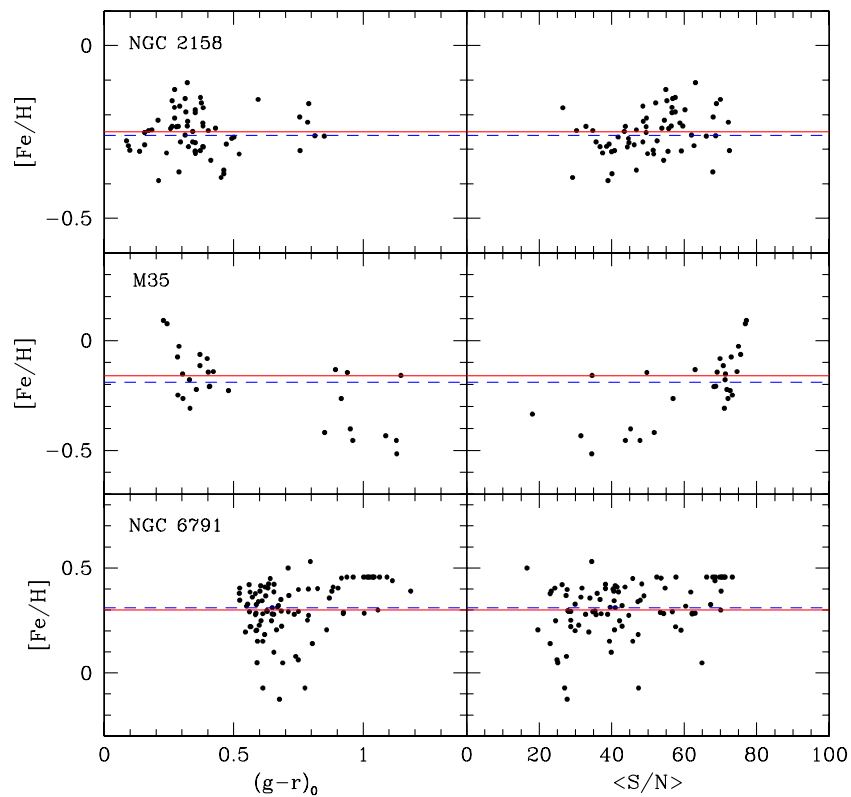

Figure 15. Same as Figure 8, but for NGC 6791.

(A color version of this figure is available in the online journal.)

Figure 16. Distribution of [Fe/H] as a function of $(g - r)_0$ (left-hand column) and average signal to noise (right-hand column) for selected true member stars of the globular clusters NGC 5053, M92, M53, M3, and M71, ordered from top to bottom on increasing metallicity. The red solid line in each panel represents the adopted value of [Fe/H] for each cluster from the Harris (1996) catalog, the black dot-dashed line is [Fe/H] from the Carretta et al. (2009) re-calibration, and the dashed blue line represents the mean measured value of each cluster.

(A color version of this figure is available in the online journal.)

Figure 17. Same as Figure 16, but for the open clusters NGC 2158, M35, and NGC 6791, ordered from top to bottom according to increasing metallicity.

(A color version of this figure is available in the online journal.)
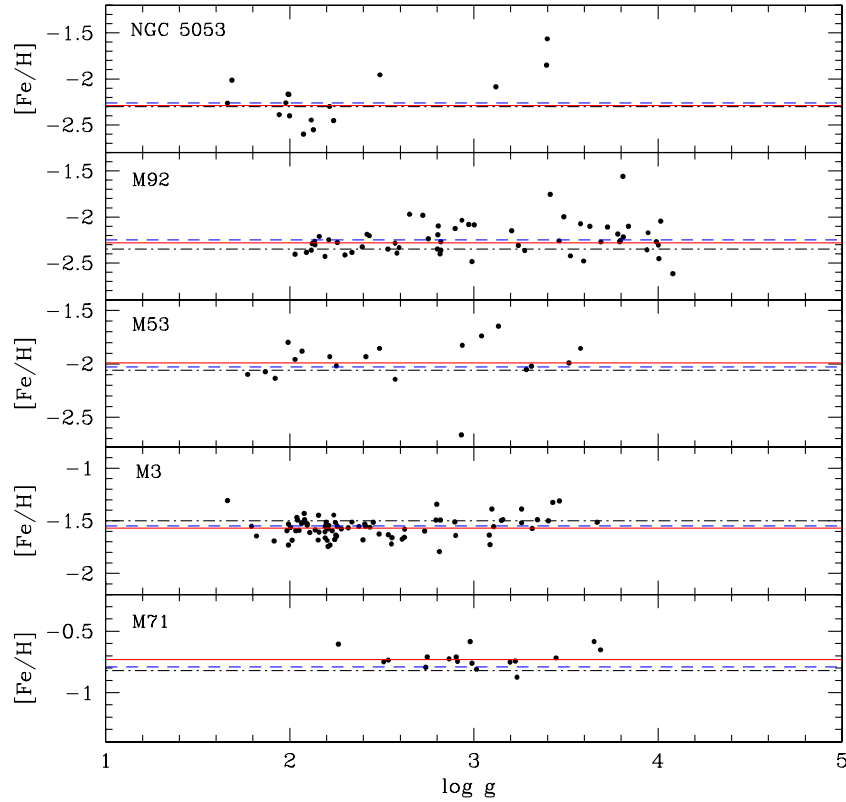
Figure 18. Distribution of [Fe/H] as a function of estimated log *g* for the selected true member stars of the globular clusters NGC 5053, M92, M53, M3, and M71, ordered from top to bottom according to increasing metallicity. As in Figure 16, the red solid line corresponds to the adopted value for [Fe/H] for each cluster from Harris (1996), the black dot-dashed line is [Fe/H] from the re-calibrated metallicity scale of Carretta et al. (2009), and the dashed blue is the mean measured value.
(A color version of this figure is available in the online journal.)

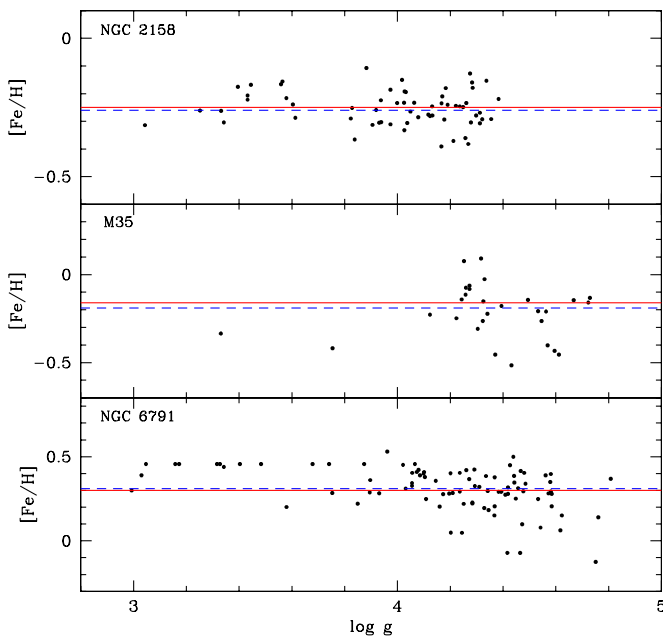**Figure 19.** Distribution of [Fe/H] as a function of estimated log *g* for the selected true member stars of the open clusters NGC 2158, M35, and NGC 6791, ordered from top to bottom according to increasing metallicity. As in Figure 16, the red solid line corresponds to the adopted literature value for [Fe/H] for each cluster, while the dashed blue is the mean measured value.
(A color version of this figure is available in the online journal.)

extinction-corrected *ugriz* magnitudes and errors for the photometry employed.

5. INDIVIDUAL CLUSTER DISCUSSION AND COMPARISON WITH PREVIOUS STUDIES

Here, we examine previous studies of these clusters and assess how well the SSPP-derived estimates for cluster metallicity and RV compare with the values reported in the literature. This section is not intended to be a comprehensive review, but rather concentrates on high-resolution spectroscopic results from studies that have been published within the past decade.[8] Due to the relative paucity of RVs for some clusters, older studies are cited where needed. We first consider the GCs, followed by the OCs, ordered from low metallicity to high metallicity.

5.1. NGC 5053

NGC 5053 is known to be metal-poor, but has otherwise not been widely studied. One spectroscopic plug-plate observation produced only 16 true member stars, with less than optimal coverage inside r_t (see Figure 1). Our estimate of the mean metallicity, $\langle[Fe/H]\rangle = -2.25 \pm 0.25$, is within 1σ of that reported by Harris (1996; -2.29). The re-calibration by Carretta et al. (2009) reports a value of -2.30, with which we are also consistent.

Our mean radial velocity, $\langle RV \rangle = +44.0 \pm 4.9\,\mathrm{km\,s^{-1}}$, is the same as that given by Harris (1996; $+44.0\,\mathrm{km\,s^{-1}}$).

5.2. M92 (NGC 6341)

Two spectroscopic plug-plate observations of this cluster yielded 58 true cluster members. Our estimated mean metal-

---

[8]   All references to Harris (1996) refer to the 2003 update on his Web site: http://www.physics.mcmaster.ca/~harris/mwgc.dat.
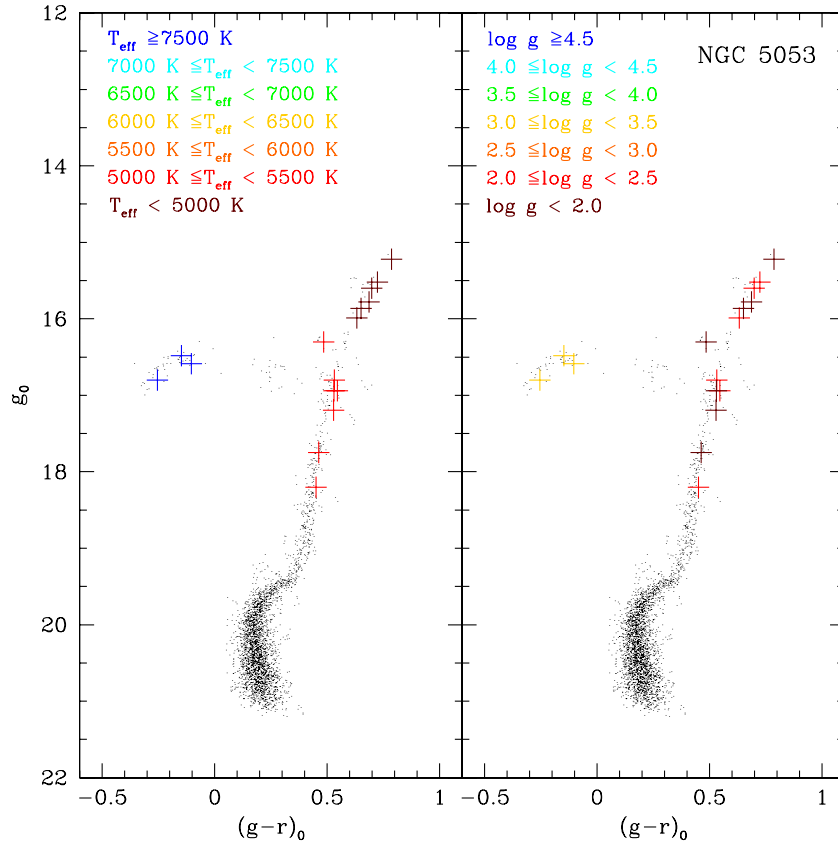
Figure 20. Color–magnitude diagram of the selected true member stars of NGC 5053. The left-hand panel shows the distribution of effective temperatures, while the right-hand panel shows the distribution of surface gravity, both based on the spectroscopic sample. The black dots are the likely member stars from the photometric sample. Each color represents a temperature step of width 500 K and a log g step of 0.5 dex, respectively.

licity, $\langle[\text{Fe/H}]\rangle = -2.25 \pm 0.17$, is within 1σ of the values given by Harris (1996; -2.28) and Carretta et al. (2009; -2.35). While King et al. (1998) obtained a much lower metallicity estimate from only Fe I lines of six subgiant stars in their sample ([Fe/H] = -2.52), examining the 17 subgiant member stars from this cluster in our sample reveals a mean metallicity of -2.27, in agreement with our overall mean metallicity as well as with the metallicities adopted by the Harris and Carretta et al. compilations. King et al. (1998) acknowledge that their low signal-to-noise spectra and limited spectral coverage, along with the metal-poor nature of M92 and an uncertain reddening correction, resulted in a degeneracy between their estimates of T_{eff} and microturbulence that may have produced a lower value for [Fe/H]. In their analysis of literature data, Kraft & Ivans (2003) report abundances from Fe I and Fe II lines of -2.50 and -2.38, respectively; both are lower than our result but consistent with King et al. (1998).

Our SSPP-derived estimate for the radial velocity, $\langle\text{RV}\rangle = -116.5 \pm 8.7 \, \text{km s}^{-1}$, is within 1σ of that provided by Harris (1996; -120.3 km s^{-1}). A recent study by Drukier et al. (2007) reported a radial velocity of RV = -121.2 km s^{-1}, based on a sample of 306 cluster members, which is also in agreement with our value.

5.3. M53 (NGC 5024)

M53 is located at the edge of the plug-plates for observations of NGC 5053, resulting in just 50 fibers being placed inside the tidal radius. As a result, only 19 stars were selected as true members. Our measured mean metallicity, $\langle[\text{Fe/H}]\rangle = -2.03 \pm 0.13$, is in agreement with Harris (1996; -1.99) and Carretta et al.

(2009; -2.06), as well as with most earlier photometric and spectroscopic abundance studies that indicated a metallicity lower than -1.8 (e.g., Pilachowski et al. 1983). More recently, a moderate-resolution spectroscopic analysis of member stars from M53 by Lane et al. (2010) provided a metallicity estimate of $\langle[\text{Fe/H}]\rangle = -1.99$, with which our result agrees nicely. Although a recent photometric study by Dékány & Kovács (2009) exhibited a discrepancy in [Fe/H] between HB (variable) stars and stars on the RGB, our sample shows no statistically significant difference between the mean metallicity on the HB versus the RGB for this cluster ($\langle[\text{Fe/H}]\rangle_{\text{HB}} = -2.11 \pm 0.09$; $\langle[\text{Fe/H}]\rangle_{\text{RGB}} = -1.96 \pm 0.12$). Our derived mean metallicity is within 1σ of their giant-branch mean metallicity of -2.12.

RV measurements reported in the literature for this cluster are a bit more scattered. Harris (1996) reported a value of -79.1 km s^{-1}, whereas a more recent medium-resolution spectroscopic study by Lane et al. (2009), using 180 giant stars, resulted in a mean value of -62.8 km s^{-1}. Our value, $\langle\text{RV}\rangle = -59.6 \pm 7.9$ km s^{-1}, from 19 RGB and HB stars, is consistent with the Lane et al. (2009) result.

5.4. M3 (NGC 5272)

One spectroscopic plug-plate observation for this cluster produced 77 true member stars. Our measured value of $\langle[\text{Fe/H}]\rangle = -1.55 \pm 0.13$ is well within 1σ of that reported by Harris (1996; -1.57) and the re-calibrated scale by Carretta et al. (2009; -1.50). A high-resolution spectroscopic study by Cavallo & Nagar (2000) of six giants at the tip of the RGB produced an estimate of [Fe/H] = -1.54, and an analysis of literature
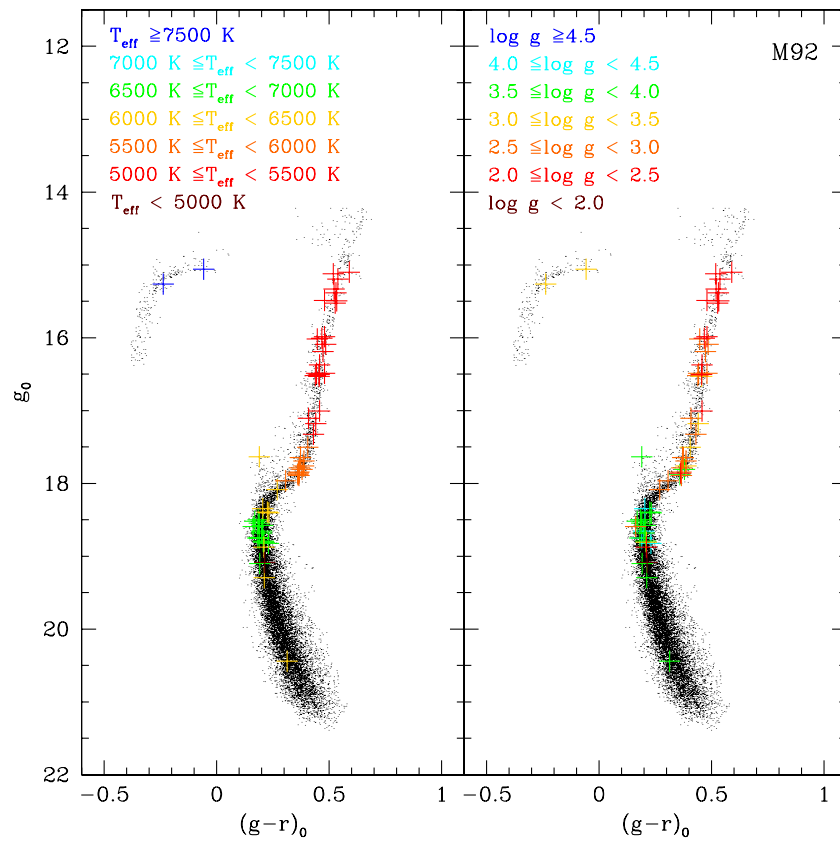
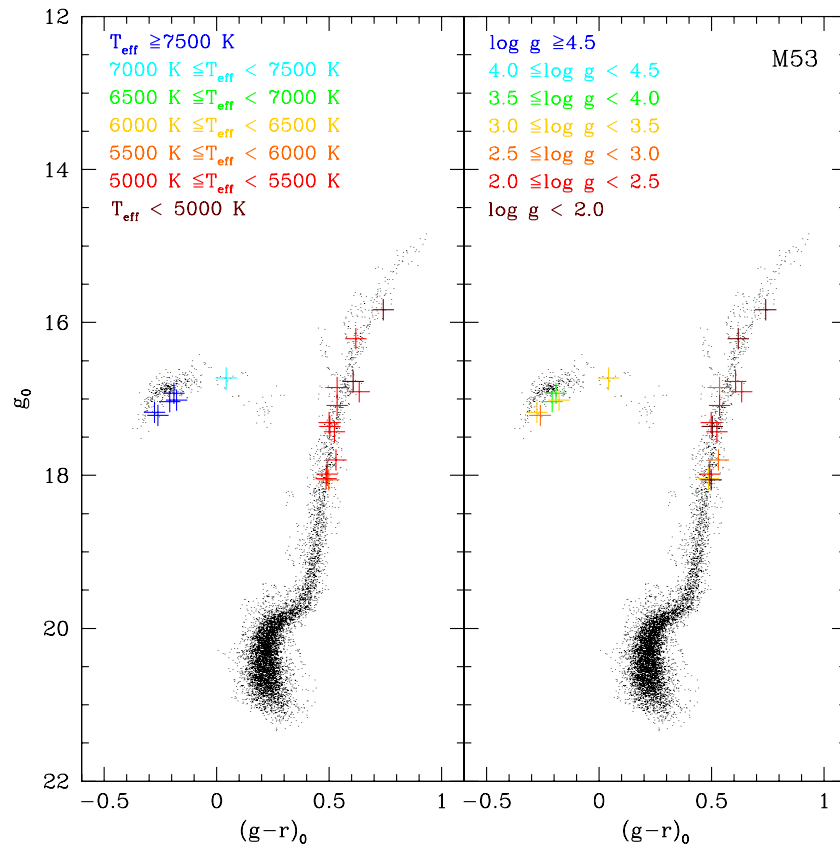**Figure 21.** Same as Figure 20, but for M92.

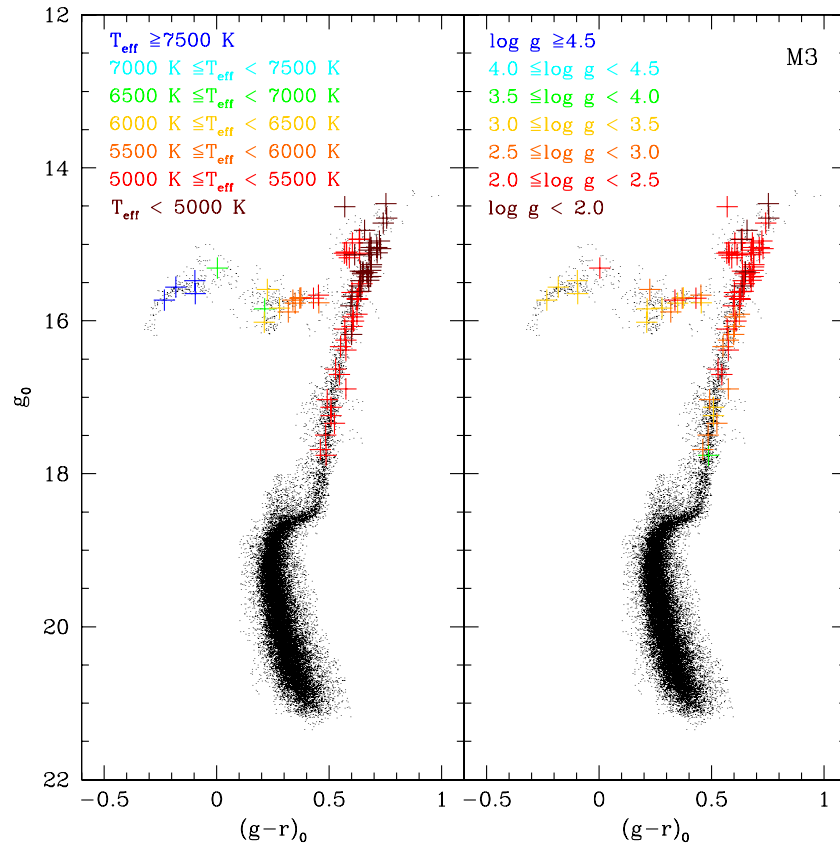**Figure 22.** Same as Figure 20, but for M53.

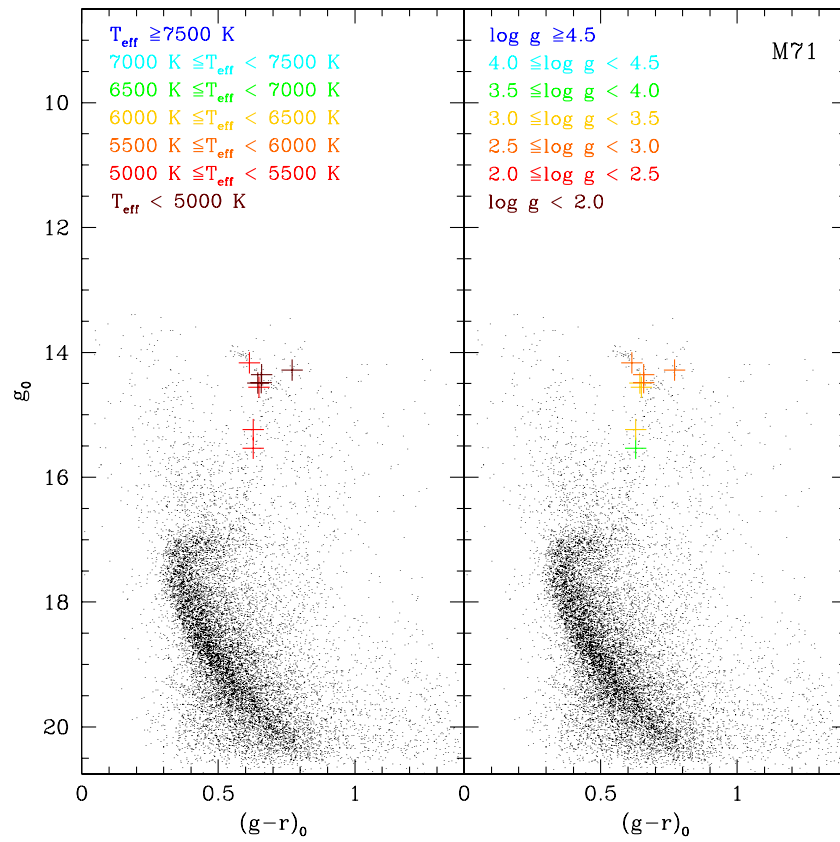**Figure 23.** Same as Figure 20, but for M3.

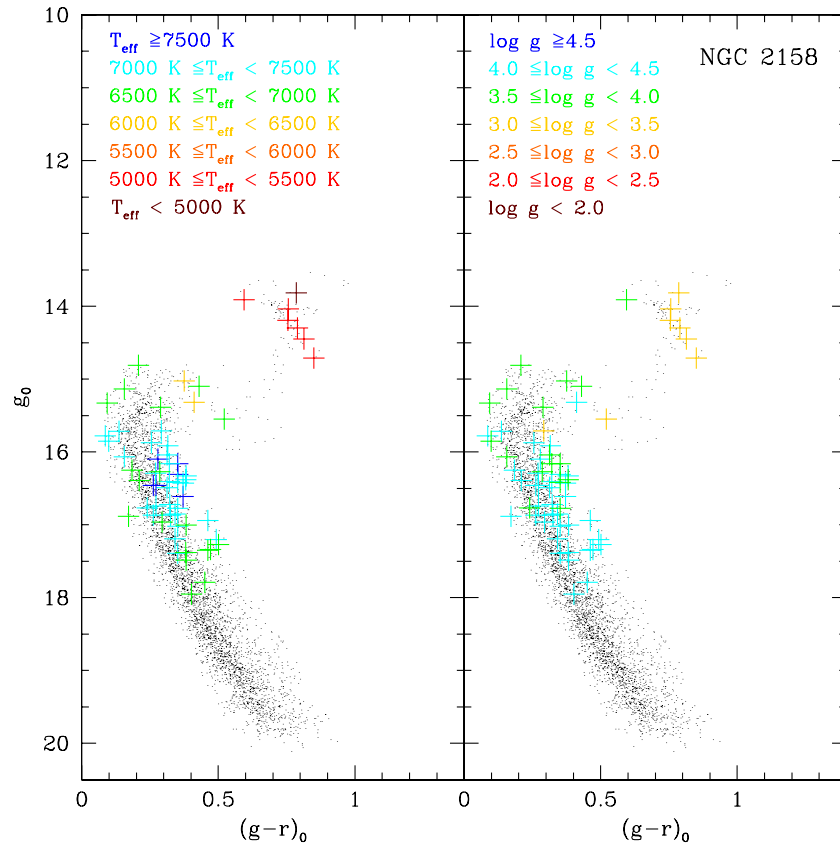**Figure 24.** Same as Figure 20, but for M71.

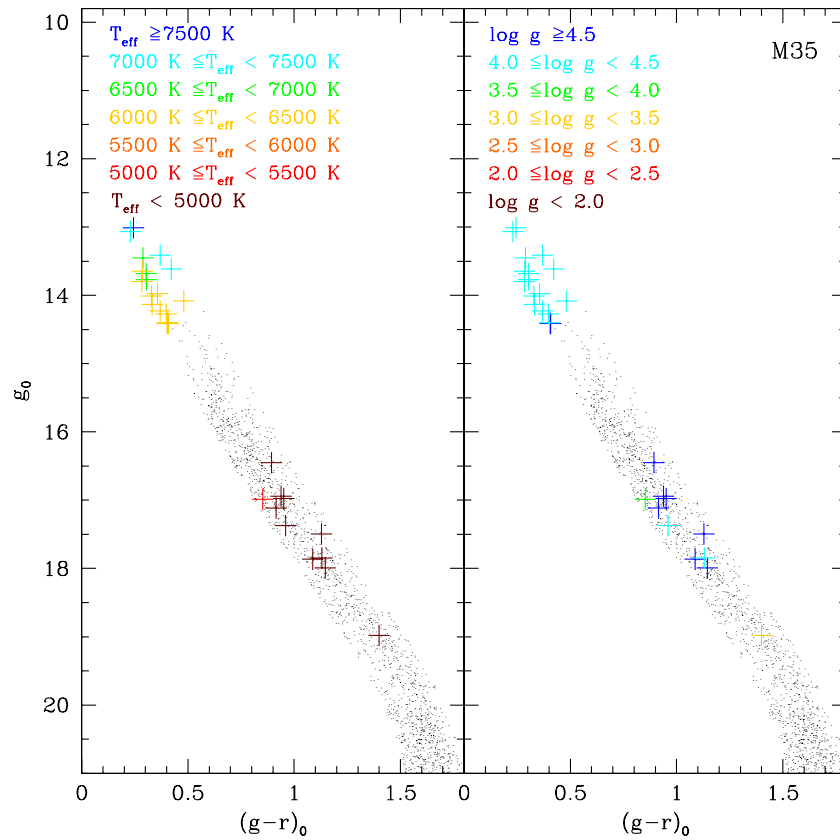**Figure 25.** Same as Figure 20, but for NGC 2158.

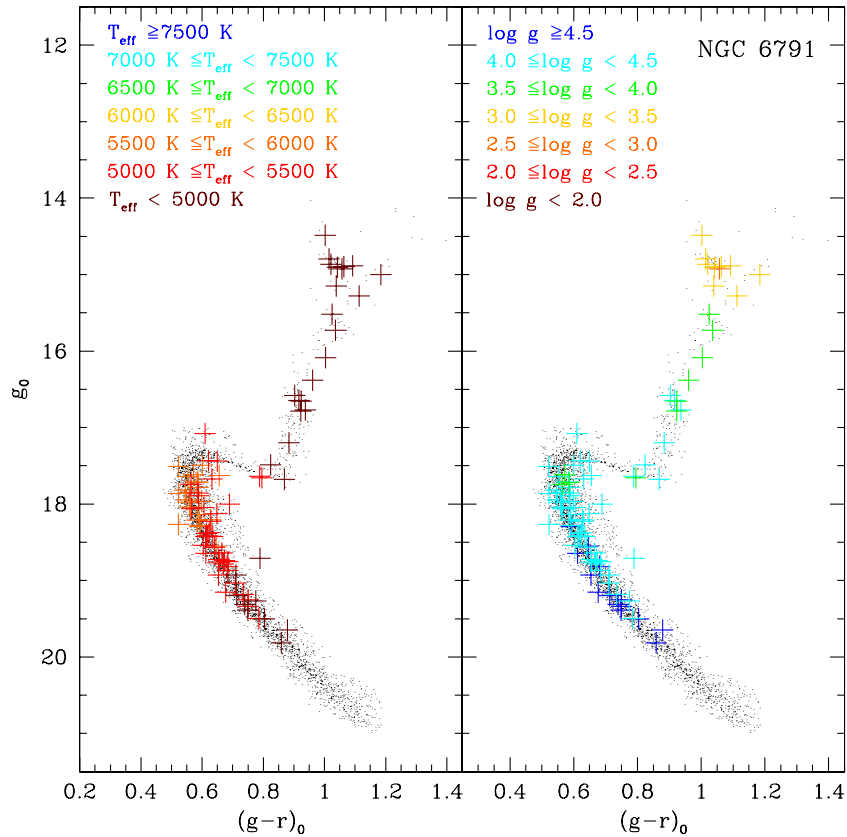**Figure 26.** Same as Figure 20, but for M35.

Figure 27. Same as Figure 20, but for NGC 6791.

data performed by Kraft & Ivans (2003) yielded metallicity estimates from both Fe I and Fe II lines of -1.58 and -1.50, respectively. Furthermore, a recent study of 23 RGB stars using high-resolution spectroscopy from Keck yielded [Fe/H] $= -1.58$ from Fe II lines (Sneden et al. 2004). Finally, while our value is only barely within 1σ of the estimated iron abundance for M3 from Cohen & Meléndez (2005), who obtained a somewhat higher value of [Fe/H] $= -1.39$ based on Keck/HIRES spectroscopy, it should be kept in mind that recent results from Cohen and collaborators adopt a temperature scale that is several hundred Kelvin warmer than most other researchers, which could easily accommodate the 0.16 dex offset with respect to their reported value of metallicity. Thus, our SSPP-derived estimate for [Fe/H] is in excellent agreement with all of these previous studies, while spanning the entire length of the RGB, including stars on the HB as well.

Our estimate of the cluster's mean radial velocity, $\langle RV \rangle = -141.2\,\mathrm{km\,s^{-1}} \pm 5.6$, is slightly different those from Harris (1996) and Cohen & Meléndez (2005), who both report the same value ($-147.6\,\mathrm{km\,s^{-1}}$), and Sneden et al. (2004) who reported a mean RV of $-149.4\,\mathrm{km\,s^{-1}}$. However, it is only just beyond 1σ of these values; when accounting for the uncertainty in the literature values the difference is not significant.

5.5. M71 (NGC 6838)

M71 is an important cluster for validation of the SSPP, due to its intermediate metallicity ([Fe/H] ~ -0.7), a regime that was not represented by previously considered clusters. Unfortunately, a total of 155 fibers inside the adopted radius of 4.0 arcmin resulted in just 17 true member stars. Literature values from Harris (1996; -0.73) and a Keck/HIRES study by Boesgaard et al. (2005; -0.80) are both consistent with our

value of the mean metallicity, $\langle[\mathrm{Fe/H}]\rangle = -0.79 \pm 0.06$, at the 1σ level, as is that from Carretta et al. (2009; -0.82). In an in-depth analysis using Keck/HIRES spectroscopy of 25 stars from the turnoff to the RHB, Ramírez et al. (2001) measured iron abundances from Fe I and Fe II lines individually, and compared them against each other for various regions of the CMD. Their values range from -0.64 to -0.86, with an error-weighted mean of -0.71, in agreement with our value at the 1.5σ level. Finally, Kraft & Ivans (2003) also report consistent abundances from Fe I and Fe II lines of -0.82 and -0.81, respectively.

Our mean RV determination, $\langle RV \rangle = -16.9 \pm 9.3\,\mathrm{km\,s^{-1}}$, is within 1σ of that reported by Harris (1996; $-22.8\,\mathrm{km\,s^{-1}}$). Keck/HIRES data from Cohen et al. (2001) produced a mean RV of $-21.7\,\mathrm{km\,s^{-1}}$, which is also consistent with our observation.

5.6. NGC 2158

A total of 109 fibers located inside the adopted radius for this open cluster (6.0 arcmin) resulted in a relatively high yield of 62 true member stars. With this sample, we measured a mean metallicity of $\langle[\mathrm{Fe/H}]\rangle = -0.26 \pm 0.08$. While this is in agreement with the values from Dias et al. (2002; -0.25), a high-resolution spectroscopic study of one giant star by Jacobson et al. (2009) produced a nearly solar mean metallicity of -0.03 ± 0.14. However, a more recent follow-up study using WIYN Hydra spectroscopy at $R \sim 21,000$ for 15 stars in NGC 2158 produced a metallicity of [Fe/H] $= -0.28 \pm 0.05$ (H. Jacobson et al. 2011, in preparation), a value that is consistent not only with prior studies of this cluster, but with ours as well.

Using moderate-resolution spectroscopy, Scott et al. (1995) reported a mean RV for NGC 2158 of $+28.1\,\mathrm{km\,s^{-1}}$. This and the value reported by Dias et al. (2002) of $+28.0$ are both consistent with our measurement of $+27.8 \pm 5.9\,\mathrm{km\,s^{-1}}$.

Table 4
Properties of Adopted True Member Stars

spSpec name	α (deg)	δ (deg)	RV (km s^{-1})	σ_{RV} (km s^{-1})	T_{eff} (K)	$\sigma_{T_{eff}}$ (K)	log g	$\sigma_{\log g}$ (dex)	[Fe/H]	$\sigma_{[Fe/H]}$ (dex)	u	σ_u	g	σ_g	r	σ_r	i	σ_i	z	σ_z	$\langle S/N \rangle$	Tag
									NGC 5053													
2476-53826-486	199.04518	17.60554	46.8	6.4	5287	101	1.99	0.47	−2.41	0.04	18.887	0.022	17.746	0.009	17.284	0.009	17.078	0.012	16.978	0.020	17.5	D
2476-53826-488	199.09269	17.69851	42.5	2.2	4951	87	2.00	0.21	−2.14	0.06	17.349	0.013	15.780	0.017	15.094	0.007	14.797	0.011	14.656	0.011	49.1	D
2476-53826-490	199.07441	17.62914	37.0	4.3	8452	171	3.08	0.28	−2.10	0.03	17.806	0.013	16.483	0.015	16.631	0.009	16.782	0.008	16.835	0.016	30.0	D
2476-53826-497	199.08809	17.59394	36.2	9.8	5397	87	2.46	0.10	−1.90	0.08	19.352	0.031	18.201	0.011	17.750	0.015	17.562	0.011	17.483	0.019	12.4	D
2476-53826-501	199.16802	17.67369	43.4	2.6	4973	52	2.11	0.25	−2.56	0.07	17.417	0.010	15.988	0.008	15.356	0.005	15.073	0.012	14.942	0.011	48.4	D
2476-53826-505	199.19265	17.70156	46.8	3.3	5353	63	1.93	0.28	−2.37	0.04	17.522	0.015	16.302	0.009	15.817	0.008	15.600	0.015	15.520	0.015	39.6	D
2476-53826-506	199.15790	17.64537	46.8	5.0	8072	116	3.51	0.23	−1.76	0.08	17.793	0.019	16.589	0.012	16.693	0.008	16.745	0.013	16.830	0.022	29.4	D
2476-53826-507	199.18189	17.62503	37.7	4.2	5126	65	1.97	0.20	−2.26	0.06	18.181	0.018	16.939	0.009	16.409	0.007	16.161	0.018	16.049	0.015	30.6	D
2476-53826-508	199.18986	17.64430	43.0	3.5	5125	61	2.20	0.16	−2.32	0.03	18.104	0.019	16.803	0.009	16.271	0.010	16.013	0.014	15.892	0.012	33.5	D
2476-53826-519	199.10217	17.66400	45.6	1.5	4965	35	1.65	0.17	−2.01	0.01	17.003	0.012	15.223	0.011	14.436	0.014	14.144	0.010	13.966	0.014	62.9	D

Notes. SSPP-derived properties of the true member stars selected from all clusters in our sample. Column 1 lists the spSpec name, which identifies the star on the spectral plate in the form of spectroscopic plug-plate number (four digits), Modified Julian Date (five digits) and fiber used (three digits). For details on how the uncertainties in these parameters are estimated, see Paper I. Values with an ellipsis were problematic and have been omitted. The final column indicates whether photometric values were drawn from "Best" photometry (B), the "Uber calibration" (U), the CASJOBS database (C), or the DAOPHOT crowded-field reduction (D).

(This table is available in its entirety in machine-readable and Virtual Observatory (VO) forms in the online journal. A portion is shown here for guidance regarding its form and content.)

Table 5
Comparison of Estimated Cluster Parameters by SSPP-7 and SSPP-P8

Cut	Cluster	$\langle[Fe/H]\rangle_7$ (dex)	$\sigma([Fe/H])_7$ (dex)	$\langle RV\rangle_7$ (km s^{-1})	$\sigma(RV)_7$ (km s^{-1})	N_7	$\langle[Fe/H]\rangle_{P8}$	$\sigma([Fe/H])_{P8}$ (dex)	$\langle RV\rangle_{P8}$ (km s^{-1})	$\sigma(RV)_{P8}$ (km s^{-1})	N_{P8}	$[Fe/H]_H$	RV_H (km s^{-1})	$[Fe/H]_{HR}$
		(1)	(2)	(3)	(4)	(5)	(6)	(7)	(8)	(9)	(10)	(11)	(12)	(13)	(14)
[Fe/H] and RV														
	M15	−2.19	0.17	−108.2	11.7	98	−2.31	0.21	−109.0	11.5	98	−2.26	−107.0	−2.33
	M2	−1.52	0.18	−2.1	9.8	76	−1.61	0.13	−2.2	10.3	71	−1.62	−5.3	−1.66
	M13	−1.59	0.13	−244.8	8.8	293	−1.63	0.13	−244.8	8.7	293	−1.54	−245.6	−1.58
	NGC 2420	−0.38	0.10	+75.1	5.9	163	−0.31	0.11	+75.0	5.9	164	⋯	+75.5	−0.37
	M67	−0.08	0.07	+34.9	4.1	52	−0.01	0.08	+35.0	3.4	75	⋯	+32.9	+0.05
RV														
	M15	−2.19	0.18	−108.4	12.2	110	−2.31	0.22	−108.5	11.4	1107	−2.26	−107.0	−2.33
	M2	−1.51	0.18	−1.8	10.3	82	−1.61	0.14	−2.0	10.7	82	−1.62	−5.3	−1.66
	M13	−1.59	0.13	−244.8	8.9	319	−1.63	0.14	−244.9	8.8	319	−1.54	−245.6	−1.58
	NGC 2420	−0.38	0.11	+75.1	6.0	171	−0.31	0.11	+75.1	6.0	172	⋯	+75.5	−0.37
	M67	−0.08	0.07	+34.8	5.8	56	−0.01	0.08	+34.9	5.5	78	⋯	+32.9	+0.05

Notes. Comparison of SSPP-estimated parameters from Paper II, which used the DR7 version of the SSPP (SSPP-7), with those produced by the pre-DR8 version (SSPP-P8). Columns 2–6 list parameters yielded by SSPP-7 and Columns 7–11 list parameters yielded by SSPP-P8. Columns 12 and 13 contain literature values from Harris (1996, Columns 12 and 13), while values from high-resolution spectroscopy reported by Carretta et al. (2009; M15, M13, and M2) and Randich et al. (2006; M67) are listed in Column 14. The value given in Column 14 for NGC 2420 (Anthony-Twarog et al. 2006) is derived from Stromgren photometry, not high-resolution spectroscopy, whereas H. Jacobson et al. (2011, in preparation) report a metallicity result from high-resolution spectroscopy of −0.22. Moderate improvement in the [Fe/H] estimates is seen at both lower and higher metallicities. The upper section of the table contains estimates based on a final true member cut using both [Fe/H] estimates as well as radial velocities, whereas the lower section contains estimates based on a final cut using radial velocities alone.

5.7. M35 (NGC 2168)

This OC is located at the edge of the plug-plates from the spectroscopic observations and was not heavily targeted with fibers. As a result, only 72 fibers were located inside the adopted radius, yielding 29 true members. The adopted radius is less than the tidal radius due to its proximity to NGC 2158. The field region of NGC 2158 does overlap with the tidal radius of M35, but this was not problematic for several reasons. First, stars included in a field region were never considered for membership so no M35 stars would have been picked up and included in NGC 2158 as potential members. Second, the rather different RVs of the two clusters would have ensured that even if some NGC 2158 stars were considered for membership in M35, they would have been dropped during the RV cut if not previously. Finally, due to their differing positions on the CMD, any potential M35 stars included in the field region of NGC 2158 would only have served to reduce the s/n in those sub-grid boxes on the CMD of NGC 2158. These being sufficiently far from the main locus, this would not cause any complications to the member selection for NGC 2158.

Our measured mean metallicity for this cluster, $\langle[Fe/H]\rangle = -0.20 \pm 0.18$, is consistent with that from Dias et al. (2002; -0.16), as well as with the study of Barrado Y Navascués et al. (2001), who obtained $\langle[Fe/H]\rangle = -0.21$ from a high-resolution spectroscopic analysis of 39 probable cluster members.

Barrado Y Navascués et al. (2001) measured a mean RV from their sample of $\langle RV \rangle = -8.0\,km\,s^{-1}$, a value consistent with our observation (-5.0 ± 6.2 km s^{-1}). While our value of $\langle RV \rangle$ is slightly higher, compared to both their sample and the value from Dias et al. (2002; -8.2), it is still within 1σ, and therefore can be considered reliable. A more recent study by Geller et al. (2010) produced an RV of $\langle RV \rangle = -8.16\,km\,s^{-1}$ based on high-resolution spectroscopy.

5.8. NGC 6791

NGC 6791 is another important cluster for our validation exercise, because it explores the super-solar metallicity region. This is another regime that was not considered with previously observed clusters; it is the most metal-rich cluster (to date) for which we were able to obtain successful spectroscopic reductions. There were two spectroscopic plug-plate observations for the region surrounding this cluster, which yielded a total of 90 true members. While our mean metallicity estimate, $\langle[Fe/H]\rangle = +0.31 \pm 0.13$, is statistically consistent with that given by Dias et al. (2002; $+0.11$) at the 2σ level, their reported value is significantly lower than that reported by other studies. It is known that NGC 6791 is a metal-rich OC, with some estimates from high-resolution spectroscopy as high as $+0.47$ (Gratton et al. 2006). A study of 24 giant stars with medium-resolution spectroscopy yielded a metallicity estimate of $[Fe/H] = +0.32$ (Worthey & Jowett 2003), while Origlia et al. (2006) used medium-high resolution Keck/NIRSPEC spectroscopy to obtain an iron abundance of $+0.35$. Most recently, a high-resolution spectroscopic study of two MSTO stars by Boesgaard et al. (2009) yielded a value of $[Fe/H] = +0.30$. It is clear that our estimate is in better agreement with these recent high-resolution observations.

Our measured value of the mean radial velocity, $\langle RV \rangle = -47.0 \pm 6.0\,km\,s^{-1}$, is consistent with that reported by Dias et al. (2002; -57 km s^{-1}) at the 1.5σ level, as well as with that found by Origlia et al. (2006; $-52\,km\,s^{-1}$).

6. COMPARISON OF SSPP-7 WITH SSPP-P8

The SSPP has been modified slightly from the version used to produce atmospheric parameter estimates for stars in SDSS DR7; for clarity, we refer to that version as SSPP-7. We refer to the current version as SSPP-P8 (for pre-DR8), since it is anticipated that a number of additional improvements will be made prior to its application to SDSS DR8. The updates and improvements that have been made since SSPP-7 are discussed in detail in the Appendix.

The spectroscopic data from Paper II for the three Galactic GCs M2, M13, and M15, along with the two OCs M67 and NGC 2420, have been analyzed with the new version of the SSPP; results are listed in Table 5 alongside those obtained from application of SSPP-7. The upper section of this table lists results for a final cut on true members performed using both $[Fe/H]$ and RV, while the lower section shows results for a final cut using RV alone. Paper II concluded that an RV cut is sufficient for stars inside a cluster r_t to obtain reliable results; this same conclusion is supported by the SSPP-P8 results. Inspection of this table also reveals clear improvements at the low-metallicity end of the scale, as compared to literature values from Harris (1996) and high-resolution spectroscopy reported by Carretta et al. (2009), Anthony-Twarog et al. (2006), and Randich et al. (2006), in particular for M15. The results for the two higher metallicity clusters are mixed, with M67 at the high-metallicity end showing moderate improvement. H. Jacobson et al. (2011, in preparation) report a higher metallicity for NGC 2420 of $[Fe/H] = -0.22 \pm 0.07$, which shows closer agreement with our improved SSPP-P8 value.

7. SUMMARY

We have used spectroscopic and photometric data from SDSS-I and SDSS-II/SEGUE to determine mean metallicities and RVs for five Galactic GCs, M3, M53, M71, M92, and NGC 5053, as well as for three OCs, M35, NGC 2158, and NGC 6791. The data were run through the current version of the SSPP (which is similar to that which will be used for the next public release, DR8), and true member stars were selected from each cluster. The derived $\langle[Fe/H]\rangle$ and $\langle RV \rangle$ for the true members were then compared to the cluster properties reported in the literature.

The mean values of $[Fe/H]$ and RV for each cluster from the SSPP are in good agreement with those values reported in previous studies. Nearly all of the SSPP estimates are within 1σ of the adopted literature values, with the exceptions almost all falling within 2σ. The mean internal uncertainties of the SSPP-determined metallicities and RVs for true members in our sample are $\sigma_{[Fe/H]} = 0.05$ dex and $\sigma_{RV} = 3.0\,km\,s^{-1}$, respectively, while the scatter about the mean residuals compared to the adopted literature values are $\sigma_{[Fe/H]} = 0.11$ dex and $\sigma_{RV} = 5.2\,km\,s^{-1}$, demonstrating good internal and external consistency, and indicating that estimates of the atmospheric parameters and RVs for SDSS/SEGUE stellar data are sufficiently accurate for use in studies of the chemical compositions and kinematics of stellar populations in the Galaxy.

APPENDIX

CHANGES IN SSPP-7 IN PREPARATION FOR SSPP-8

In the period since SDSS Data Release 7 (DR7; Abazajian et al. 2009), the SEGUE Stellar Parameter Pipeline (SSPP; Paper I) has evolved somewhat, in order to improve our estimates of the stellar parameters $T_{\rm eff}$, $\log g$, and [Fe/H]. In the version of the SSPP used for DR7, there were six primary temperature estimates and an auxiliary set of five empirically and theoretically determined estimates. For surface gravity estimation, 10 methods were employed. Twelve different methods were employed to determine [Fe/H]. Depending on a star's $(g - r)_0$ and the S/N of the spectrum, an indicator variable (taking on values of 0 or 1) was assigned for each technique used for a given parameter estimate. Following application of a parameter decision tree, all available estimates from individual methods for each parameter were combined to yield final adopted values. Details on each method and the decision tree for each parameter can be found in Paper I.

At the time the DR7 version of the SSPP was constructed there existed a dearth of metal-rich ([Fe/H]> 0.0) and metal-poor ([Fe/H]< -3.0) stars available as calibrators, hence the metallicity determinations at the extrema were not well constrained. Since then, we have obtained data for more metal-poor and metal-rich clusters, including the important clusters M92 and NGC 6791, and also secured more SDSS/SEGUE stars with available high-resolution spectroscopy. These enabled substantial improvement in parameter estimates for SDSS/SEGUE stellar spectra.

Here, we highlight major and minor changes that have been made on the SSPP since the DR7 version; the new version of the SSPP is referred to as SSPP-P8, as a version similar to this will be used for application to Data Release 8 (DR8), scheduled for 2011 January. The version of the SSPP used for DR7 is referred to as SSPP-7. Here, *major change* indicates that the modification described directly affects the parameter estimation for each method, and hence the final adopted value, whereas *minor change* indicates that the modification does not influence parameter estimation, but helps to more easily identify peculiar

behavior in the observed spectra, or possibly the presence of ill-measured parameters.

A.1. Major Changes in the SSPP

Since there are no substantial changes in the methodology for estimating $T_{\rm eff}$ and $\log g$, or in the averaging scheme employed to obtain final adopted values, we focus on modifications made to obtain improved metallicity estimates. However, note that the final adopted value of $T_{\rm eff}$ and $\log g$ estimates are slightly different in SSPP-P8, due to the re-calibration of the NGS1 and NGS2 approaches, and to some additional changes in the validity ranges of S/N and $(g - r)_0$. The basic ideas for deciding which estimator goes in the final averaging stage for those two parameters and the nomenclature for each method can be found in Paper I.

A.1.1. Changes in S/N and $(g - r)_0$ Ranges for Individual Methods

The valid ranges of S/N and $(g - r)_0$ for each method mostly remain the same as before, but the color range for application of the WBG method is substantially narrowed, since it is based on a grid of synthetic spectra that only extends to [Fe/H] = 0.0, thus it is not applicable for the full range of expected metallicities for metal-rich G- and K-type stars. In SSPP-7, its use lowered the overall metallicity estimates for stars with super-solar metallicity ([Fe/H] > 0.0). Table A1 summarizes the current status of the S/N and $(g - r)_0$ ranges for individual methods.

A.1.2. Re-calibration of the NGS1 and NGS2 Methods

The NGS2 method implements a dense and extended grid of synthetic spectra, spanning from 4000 K $\leqslant T_{\rm eff} \leqslant$ 8000 K in steps of 250 K, $0.0 \leqslant \log g \leqslant 5.0$ in steps of 0.2 dex, and $-4.0 \leqslant$ [Fe/H] $\leqslant +0.4$ in steps of 0.2 dex. The [α/Fe] ratio covers from $-0.1 \leqslant$ [α/Fe] $\leqslant +0.6$ at each node of $T_{\rm eff}$, $\log g$, and [Fe/H]. Details on the models used to generate the synthetic spectra are described in Paper I.

A linear flux interpolation routine has been added to the NGS1 approach in order to generate synthetic spectra in finer steps of 125 K, 0.125 dex, and 0.1 dex for $T_{\rm eff}$, $\log g$, and [Fe/H], respectively, using the existing NGS1 grid, before χ^2 minimization calculations are carried out. This provides a tighter parameter search space for the χ^2 minimization scheme for the NGS1 technique than previously.

Following these adjustments, metallicity estimation of the NGS1 and NGS2 methods is re-calibrated using likely member stars of globular (M92, M15, M13, and M2) and OCs (NGC 2420, M67, and NGC 6791), by fitting a simple linear function of [Fe/H] to the residuals between recent literature values and the metallicity estimates from the NGS1 and NGS2 methods, after adding a metal-poor GC (M92) and a super-solar metal-rich OC (NGC 6791), which were not available at the time of the SSPP-7 calibration. The calibration procedure adopts the following metallicities: M92 ([Fe/H] = -2.35), M15 ([Fe/H] = -2.33), M13 ([Fe/H] = -1.58), and M2 ([Fe/H] = -1.66) from Table A1 in Carretta et al. (2009), NGC 2420 ([Fe/H] = -0.37) from Anthony-Twarog, et al. (2006), M67 ([Fe/H] = $+0.05$) from Randich et al. (2006), and NGC 6791 ([Fe/H] = $+0.30$) from Boesgaard et al. (2009). After re-calibration, we have obtained the following correction functions of the metallicity scale compared to the uncalibrated values:

$$[{\rm Fe/H}]_{\rm NGS1} = [{\rm Fe/H}] + 0.178 \cdot [{\rm Fe/H}] + 0.406, \qquad {\rm (A1)}$$

Table A1
Valid Ranges of $g - r$ and S/N for Individual Methods in the SSPP-P8

$T_{\rm eff}$			log g			[Fe/H]			S/N	Reference
Name	Method	$g - r$	Name	Method	$g - r$	Name	Method	$g - r$		
T1	ki13	$0.0 - 0.8$	G1	ki13	$0.0 - 0.8$	M1	ki13	$0.0 - 0.8$	$\geqslant 15$	Section 4.1
T2	k24	$0.0 - 0.8$	G2	k24	$0.0 - 0.8$	M2	k24	$0.0 - 0.8$	$\geqslant 15$	Allende Prieto et al. (2006)
T3	WBG	$-0.3 - 0.3*$	G3	WBG	$-0.3 - 0.3*$	M3	WBG	$-0.3 - 0.3*$	$\geqslant 10$	Wilhelm et al. (1999)
T4	ANNSR	$-0.3 - 0.8$	G4	ANNSR	$-0.3 - 0.8$	M4	ANNSR	$-0.3 - 0.8$	$\geqslant 20$	Section 4.3
T5	ANNRR	$-0.3 - 1.2$	G5	ANNRR	$-0.3 - 1.2$	M5	ANNRR	$-0.3 - 1.2$	$\geqslant 10$	Re Fiorentin et al. (2007)
T6	NGS1	$-0.3 - 1.3$	G6	NGS1	$-0.3 - 1.3$	M6	NGS1	$-0.3 - 1.3$	$\geqslant 10*$	Section 4.4
...	......	....	G7	NGS2	$0.0 - 1.3$	M7	NGS2	$0.0 - 1.3$	$\geqslant 20$	Section 4.4
...	......	....	G8	CaI1	$0.3 - 1.2*$	M8	CaIIK1	$-0.3 - 0.8$	$\geqslant 10$	Section 4.5
...	......	....	...	......	....	M9	CaIIK2	$0.1 - 0.8$	$\geqslant 10$	Beers et al. (1999)
...	......	....	...	......	....	M10	CaIIK3	$0.1 - 0.8$	$\geqslant 10$	Section 4.6
...	......	....	...	......	....	M11	ACF	$0.1 - 0.9$	$\geqslant 15$	Beers et al. (1999)
...	......	....	...	......	....	M12	CaIIT	$0.1 - 0.7$	$\geqslant 20$	Cenarro et al. (2001a, 2001b)
...	......	....	G9	CaI2	$0.3 - 1.2*$	...	......	....	$\geqslant 10$	Morrison et al. (2003)
...	......	....	G10	MgH	$0.3 - 1.2*$	...	......	....	$\geqslant 10$	Morrison et al. (2003)
T7	HA24	$0.1 - 0.8*$	...	......	....	...	......	....	$\geqslant 10$	Section 5.1
T8	HD24	$0.1 - 0.6*$	...	......	....	...	......	....	$\geqslant 10$	Section 5.1
T9	T_K	$-0.3 - 1.3$	...	......	....	...	......	....	N/A	Section 5.1
T10	T_G	$-0.3 - 1.3$	...	......	....	...	......	....	N/A	Section 5.1
T11	T_I	$-0.3 - 1.3$	...	......	....	...	......	....	N/A	Ivezić et al. (2008)

Notes. The symbol $*$ indicates that changes have been made in the color or S/N range. The section number listed is that from Paper I, and references therein.

$$[\text{Fe/H}]_{\rm NGS2} = [\text{Fe/H}] + 0.212 \cdot [\text{Fe/H}] + 0.417. \qquad (A2)$$

Along with the extended grid for the NGS2, this re-calibration has improved the final adopted metallicity in SSPP-P8 at both the low-metallicity (< -3.0) and high-metallicity (> 0.0) extrema.

A.1.3. A New Decision Tree for [Fe/H] Estimates

Although the basic idea of averaging the various metallicity estimates follows the decision tree implemented in SSPP-7, we have added to the averaging scheme a few more criteria to reject likely outliers.

There are 12 estimates of [Fe/H] in the SSPP-P8, as was also the case for the SSPP-7. We adopt the validity ranges of S/N and $(g - r)_0$ listed in Table A1 to assign 1 or 0 as an indicator variable for each method. We then proceed as follows. First, we generate a synthetic spectrum for each estimate of [Fe/H] that has an indicator variable of 1 (using the adopted $T_{\rm eff}$ and log g) by interpolating within the pre-existing grid of synthetic spectra from the NGS1 approach. Next, we calculate a correlation coefficient (CC) and the mean of the absolute residuals (MAR) between the observed and the generated synthetic spectrum in two different wavelength regions: 3850–4250 Å and 4500–5500 Å, where the Ca II K and H lines, as well as numerous metallic lines, are present, yielding two values of CC and MAR for each metallicity estimator. We then select between the two values by choosing the one with CC closest to unity and with MAR closest to zero. This applies for all estimates of [Fe/H] from the individual methods. At the end of this process, we have N values of the CC and MAR (maximum of $N = 12$) for the N estimates of [Fe/H] with indicator variables of 1. There are thus two arrays with N elements: one from the CC and the other one from the MAR values.

We then sort the CC array in descending order and select the metallicity estimate corresponding to the first and second element of the sorted array. The same procedure is carried out for the MAR array, after sorting in ascending order. The reason for implementing calculations involving the MARs is that, although we may have a correlation coefficient close to unity between the observed and the synthetic spectrum, from time to time there are large residuals between the two spectra, indicating a poor match. Thus, the computations involving the MAR provide additional security that the methods are producing reasonable abundance estimates at this stage.

At this point we have two metallicity estimates with the highest CCs and two metallicity estimates with the lowest MARs. We then take an average of the four metallicities and use this average to select from among the full set of metallicity estimates with an indicator variable of 1 and within ± 0.5 dex of the average. We carry along the CCs and MARs for the selected metallicity estimates for further processing.

In the next step, we obtain an average $\mu_{\rm CC}$ ($\mu_{\rm MAR}$) and standard deviation $\sigma_{\rm CC}$ ($\sigma_{\rm MAR}$) of the CCs (MARs) for the surviving metallicity estimates from the previous step. As a final step to reject likely outliers, we select from the surviving metallicity estimates the ones with the CC greater than ($\mu_{\rm CC} - \sigma_{\rm CC}$) and the MAR less than ($\mu_{\rm MAR} + \sigma_{\rm MAR}$). The metallicity estimators that remain after this step are assigned indicator variables of 2. This procedure effectively ignores metallicity estimates that produce poor matches with the synthetic spectra. The final adopted value of [Fe/H] is computed by taking a biweight average of the remaining values of [Fe/H] (those with indicator variables of 2).

Figure A1 shows comparisons of metallicity estimates from individual methods with those from the high-resolution spectroscopic analysis and confirms how well the new outlier rejection algorithm works. When inspecting such plots, it is well to keep in mind that one can assume that the high-resolution predictions of metallicity carry at least an internal error on the order of 0.1 dex, and (since they were not obtained from a uniform analysis), a user-to-user error that may be of similar magnitude when various samples are combined as we have done.

A.2. Minor Changes in the SSPP

Although the minor additions (or subtractions) to the SSPP do not alter the parameter estimations, they greatly assist the user
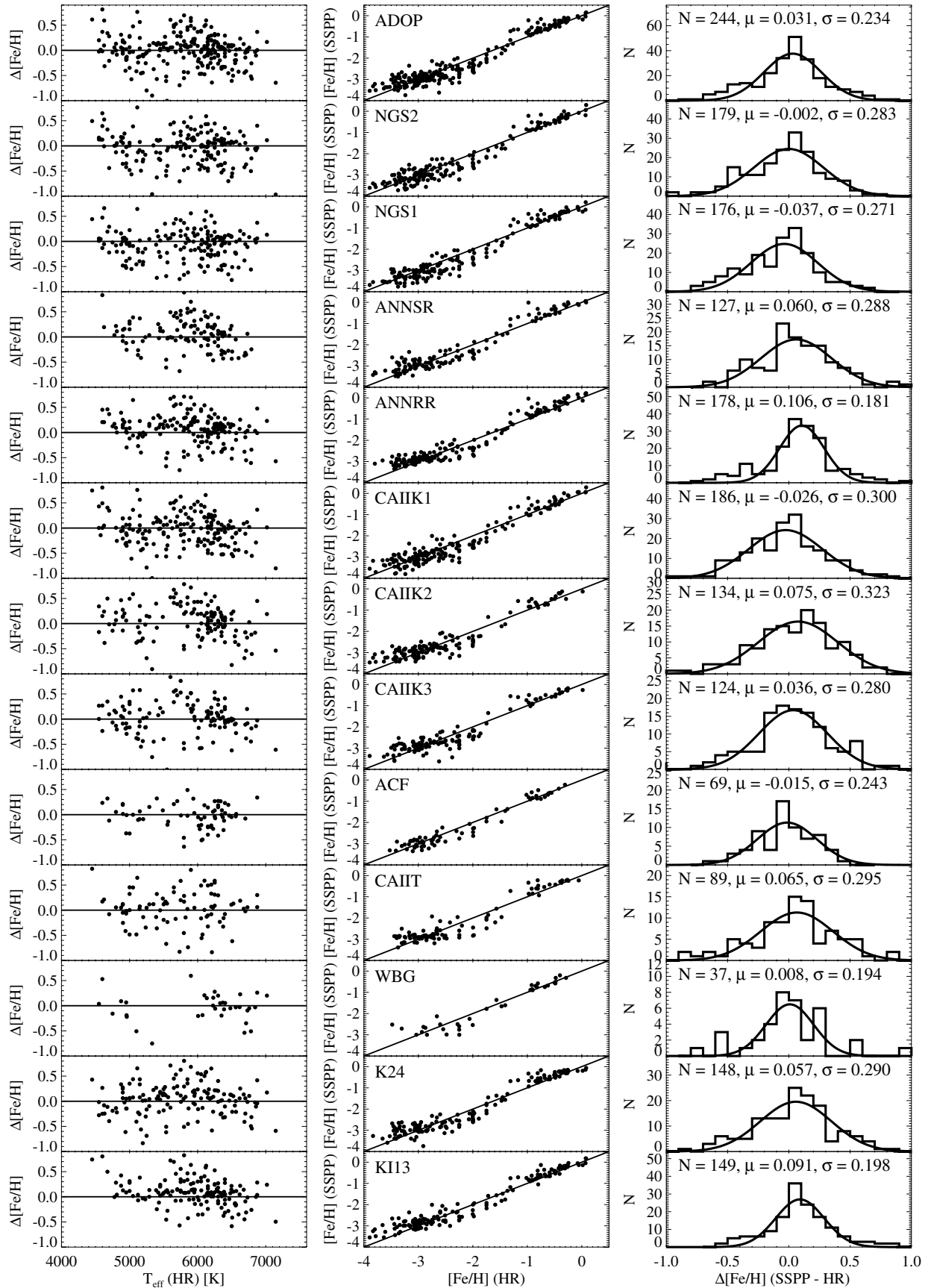
Figure A1. Metallicity comparison of the individual methods in SSPP-P8 with the metallicities obtained from high-resolution spectra. Because only the estimators with indicator variables set to two are considered (except in the case of the adopted value ADOP), the total number of the stars differs from method to method. These plots show how well the outlier rejection routine works—there are few large outliers in the individual comparisons.

Table A2
Brief Descriptions of SSPP Flags

Position	Flag	Description	Category	Parameter	Status
First					
	n	Appears normal	......	Yes	......
	D	Likely white dwarf	Critical	No	......
	d	Likely sdO or sdB	Critical	No	......
	H	Hot star with $T_{eff} > 10000$ K	Critical	No	......
	h	Helium line detected, possibly very hot star	Critical	No	......
	l	Likely late-type solar abundance star	Cautionary	Yes	......
	E	Emission lines in spectrum	Critical	No	......
	S	Sky spectrum	Critical	No	......
	V	No radial velocity information	Critical	No	......
	N	Very noisy spectrum	Cautionary	Yes	......
Second					
	n	Appears normal	......	Yes	......
	C	The photometric $g - r$ color may be incorrect	Cautionary	Yes	......
Third					
	n	Appears normal	......	Yes	......
	B	Unexpected Hα strength predicted from Hδ	Cautionary	Yes	......
	b	If d or D flag is not raised among stars with B flag	Yes	Add	
Fourth					
	n	Appears normal	......	Yes	......
	G	Strong G-band feature	Cautionary	Yes	......
	g	Mild G-band feature	Cautionary	Yes	......
Fifth					
	n	Appears normal	......	Yes	......
	P	Parameters reported for $5.0 \leqslant$ S/N < 10.0	Cautionary	Yes	Drop
	N	No parameters	Critical	No	Drop
	B	Too blue $((g - r)_0 < -0.3)$ to estimate parameters	Critical	No	Add
	R	Too red $((g - r)_0 > 1.3)$ to estimate parameters	Critical	No	Add
	X	No parameters estimated	Critical	No	Add
	c	Correlation coefficient < 0.4	Cautionary	Yes	Add
	T	Different between adopted T_{eff} and $(g - z)_0$-based $T_{eff} > 500$ K	Cautionary	Yes	Add
	P	Possible predicted $(g - r)_0$ is wrong	Cautionary	Yes	Add
RV					
	NORV	No radial velocity information	......	No	......
	ELRV	Radial velocity from ELODIE template	......	Yes	......
	BSRV	Radial velocity from `spectro1d`	......	Yes	......
	RVCAL	Radial velocity calculated from SSPP	......	Yes	......

Notes. No parameters are reported when "Critical" flags are raised.

interested in being made aware of peculiarities in the spectra or poorly determined parameters.

A.2.1. A New Color-based Temperature Estimate

It has proven useful to provide a new estimated T_{eff} based on $(g - z)_0$, as it has a longer baseline than other colors (e.g., $(g - r)_0$). This is especially useful for redder stars. After a careful calibration procedure using likely cluster members and the high-resolution calibration stars, we have derived the following two color–temperature relations, which are applicable over two different metallicity ranges.

For [Fe/H] < -1.5,

$$T_{eff} = 6993 - 2573 \cdot (g - z)_0 + 530.9 \cdot (g - z)_0^2 \qquad (A3)$$

and for [Fe/H] $\geqslant -1.5$,

$$T_{eff} = 6947 - 2480 \cdot (g - z)_0 + 509.3 \cdot (g - z)_0^2. \qquad (A4)$$

The typical error in T_{eff} is less than 200 K for a dwarf with an uncertainty of 0.1 mag in $(g - z)_0$.

A.2.2. χ^2 Minimization with Fixed T_{eff} from $(g - z)_0$

Another set of [Fe/H] and log g estimates are obtained from NGS1, NGS2, and CaIIK1, by minimizing χ^2 over [Fe/H] and log g after fixing the temperature determined from the $(g - z)_0$ approach described above. In this procedure, the Hβ line is masked out for the NGS1 and NGS2 methods. These parameters are derived as a check on the parameters of the metal-poor cool giants, for which the SSPP derives slightly higher temperatures (about 200 K) and higher metallicities (about 0.3 dex), as compared to the high-resolution analysis of the ESI spectra (Lai et al. 2009). For now, these parameters are not considered in the final averaging step.

A.2.3. Flux Interpolation Scheme

Since spline interpolation exhibits finer absorption features than the linear interpolation approach, the former is employed to obtain fluxes in the linear wavelength scale used by the SSPP than is derived from the SDSS logarithmic wavelength scale. The synthetic spectra for the NGS1 and NGS2 grids are also treated in the same fashion.
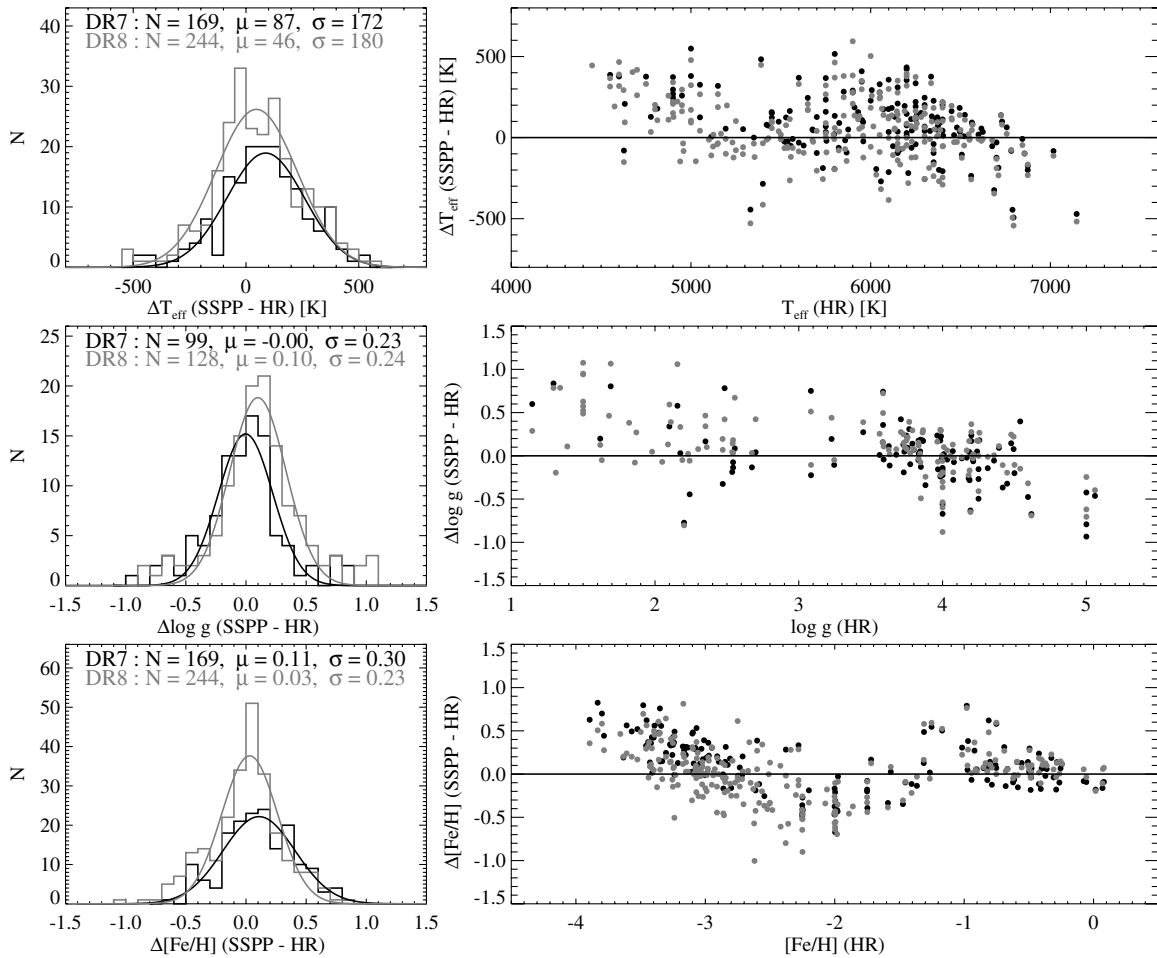
Figure A2. Comparison of SSPP-7 with SSPP-P8 for the high-resolution calibration stars. The gray dots and lines are associated with SSPP-P8, while the black dots and lines correspond to SSPP-7. Although there are still outliers, overall there is substantial improvement in estimation of [Fe/H] in SSPP-P8, as can be seen at the top of the lower-right panel. The offset is reduced by 0.08 dex and the scatter by 0.07 dex from SSPP-7 to SSPP-P8. Note that the high-resolution results are (unfortunately) not all derived in a homogeneous manner, a defect that hopefully will be remedied soon, based on work in progress. In particular, we believe that the "waves" in the metallicity estimates arise, not due to inconsistencies in the SSPP, but rather, due to the inhomogeneous high-resolution analyses.

A.2.4. Spectroscopy-based Parameters

We have chosen to output another set of adopted T_{eff}, log g, and [Fe/H] estimates, following the same decision tree as before, but only including individual estimates for which reported colors (e.g. $(g - r)_0$) are not involved in the process of their determination. These parameters are useful to compare with the final adopted parameters for cases where the reported colors are suspicious, just wrong, or highly reddened.

A.2.5. New Flags for Visual Inspection

A flag based on a six letter combination is added to speed up the visual inspection of the stellar spectra. Those spectra where one or more of these flags are raised are visually inspected, while those with no flags raised ("nnnnnn") can be safely assumed to be OK.

Definitions for each flag are as follows.

1. "n": this flag indicates nominal behavior.
2. "F": this flag is raised if there are no parameters or no radial velocity determined.
3. "T": this flag is raised if the difference in T_{eff} between the adopted and $(g - z)_0$ color-based T_{eff} is >500 K.
4. "t": this flag is raised if the difference in T_{eff} between the adopted and the spectroscopic-based T_{eff} is >500 K.

5. "M": this flag is raised if the difference in [Fe/H] between the adopted and spectroscopic-based [Fe/H] is >0.3 dex.
6. "m": this flag is raised if the error of the adopted metallicity is >0.3 dex.
7. "C": this flag is raised if the correlation coefficient is <0.4.

A.2.6. Changes on Raising Flags

There have been some flags added and some dropped among the conventional SSPP flags. Table A2 lists the flag definitions used in SSPP-P8. Refer to the sixth column of the table to see if a flag is added or has dropped out. Note that the "P" flag now has a different meaning than in SSPP-7 and the "N" flag is replaced by "X."

A.3. Comparison with High-resolution Spectroscopic Observations

In addition to the high-resolution sample used to validate SSPP-7 (Allende Prieto et al. 2008), we have continued to add to the sample of SDSS/SEGUE stars that have been observed with high-dispersion spectrographs on various large telescopes, such as HET, Keck, Subaru, and the VLT. Table A3 summarizes the current sample of the high-resolution spectroscopy for SDSS and SEGUE stars. The ESI, Subaru, and VLT data obtained since DR7 were analyzed by David Lai, Wako Aoki, and

Table A3
Updated List of High-resolution Spectra for SDSS and SEGUE Stars

Telescope	Instrument	Resolving Power	Wavelength Coverage (Å)	Number of Stars
Keck-I	HIRES	45000	4020–8450	11
Keck-II	ESI	6000	3850–10000	51
HET	HRS	15000	4130–5910	110
Subaru	HDS	45000	4020–6700	151
VLT	UVES	60000	3300–4600, 4700–6800	20

Piercarlo Bonifacio, respectively, who kindly provided their derived parameters in advance of publication.

Among about 340 stars, after removing problematic spectra, for example, those with low S/N($< 20/1$), we have 244 stars to compare with the parameters derived from SSPP-P8. Figure A2 shows a summary of these results (based on the adopted parameters only), including a comparison with SSPP-7. The gray dots and lines denote the comparisons with SSPP-P8, while the black dots and lines indicate comparisons with SSPP-7. The different total number of the stars to compare arises from the different number of high-resolution spectra available at the time of running each version of the SSPP. The reason for the much lower number of stars in the gravity comparison is that most of the Subaru spectra were analyzed under the assumption of $\log g = 4.0$ (as they are mostly turnoff stars). Therefore, they were removed in order to obtain a fair comparison. Inspection of the plots shows that there is not much change in the $T_{\rm eff}$ and $\log g$ estimates between the SSPP-7 and SSPP-P8 versions, even with the much larger sample size now available, although the overall gravity determination is shifted by about 0.1 dex toward higher values.

Even though there are some outliers below [Fe/H] < -2.0, we can see that the scatter above [Fe/H] > -1.0 and the offset below [Fe/H] < -2.5 in SSPP-P8 are smaller than those of SSPP-7. Only considering the stars with [Fe/H] > -1.0 in the comparison with the high-resolution results, we obtain a scatter of 0.14 dex for SSPP-7 and 0.12 dex for SSPP-P8, whereas for the stars with [Fe/H] < -2.5, the offsets are 0.27 dex for SSPP-7 and 0.05 dex for SSPP-P8, with a similar scatter of about 0.24 dex. The much smaller scatter and offset found for SSPP-P8 arises mainly from the extended grid for the NGS2, the re-calibration of the metallicity scale for the NGS1 and the NGS2 methods, and the new outlier rejection algorithm for computing the final adopted metallicity. It is worth noting that the "waves" in the residuals for [Fe/H] could in principle be empirically fit and calibrated out, but we have hesitated to do this until a more uniform and homogeneous set of high-resolution analyses has been carried out.

As mentioned in Appendix A.1.3, Figure A1 shows a comparison of the metallicity estimates for each method used in the present SSPP, as a function of the high-resolution estimates of temperature and metallicity. In this figure, one can clearly also see the evidence of very similar "waves" in the metallicity residuals shown in the middle column of panels, which makes us suspicious that the problem lies in the high-resolution determinations, not in the individual methods themselves, which go back to very different individual calibration approaches.

A.4. Comparison with Likely Cluster Member Stars

Two OCs (NGC 2420, M67) and three GCs (M15, M13, and M2) were used to calibrate and validate the parameters derived by SSPP-7 (Paper II). Since there was only one metal-rich cluster near solar metallicity (M67) and one metal-poor cluster
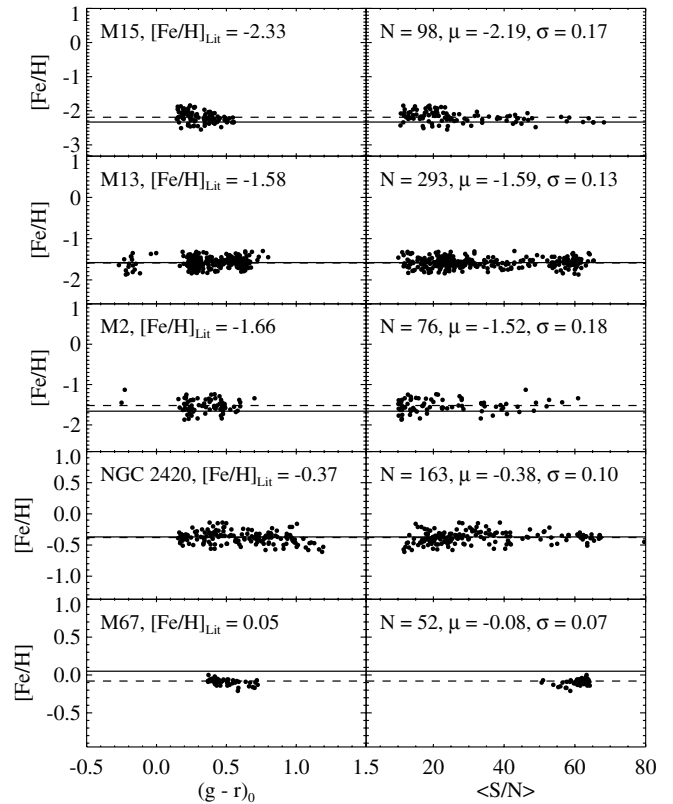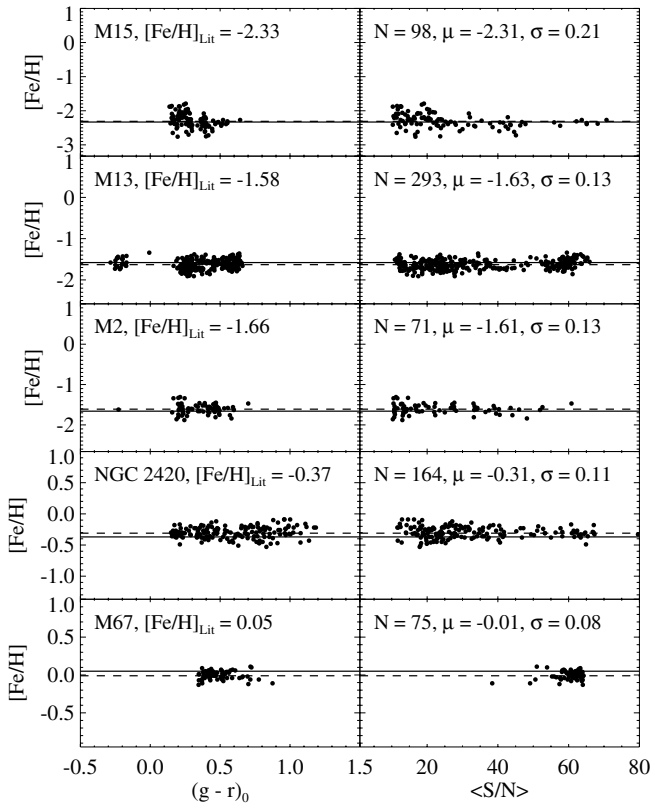

Figure A3. Comparison with true cluster member stars based on SSPP-7. The solid line indicates the literature value, while the dashed line is the average value reported by SSPP-7 for a given cluster. Note that slight offsets exist between the overall mean of SSPP-7 estimates and the literature values for M15, M2, and M67.

(M15) included, at the high-metallicity and low-metallicity ends SSPP-7 was not well calibrated, as can be seen in Figure A3. However, thanks to adding two more clusters to the list from Paper II (NGC 6791 and M92), one super metal-rich OC ([Fe/H] $= +0.3$), and another metal-poor GC ([Fe/H] $= -2.35$), respectively, we are able to re-calibrate the individual pipelines in the SSPP, with the help of the high-resolution spectra for many stars with [Fe/H] < -3.0. Figure A4 shows the results of the calibration and the comparison. One can see that at both the metal-poor and metal-rich ends, SSPP-P8 reproduces the literature values very well, throughout the entire metallicity range shown in the figure.

A.5. Summary

We have described major and minor changes made to the SSPP since the DR7 version. There are three major changes: (1) an extended grid for NGS2 has been added; (2) a re-calibration for NGS1 and NGS2 has been performed, including four GCs (M92, M15, M13, and M2) and three OCs (NGC 2420, M67, and NGC 6791), along with the aid of SDSS/SEGUE stars for which high-resolution spectra were obtained; and (3) a new outlier rejection scheme has been introduced.

With the implementation of these major changes, an overall improvement for estimation of [Fe/H] has been obtained for SSPP-P8. In particular, estimates at high and low metallicities have been much improved, compared to SSPP-7. Adopting the intrinsic error in [Fe/H] for the HET data described in Paper II as a typical internal error for the high-resolution analysis (0.049 dex), and 0.23 dex in the lower panel of Figure A2 as the SSPP-P8 metallicity error, this results with an error of 0.225 dex

Figure A4. Comparison with true cluster member stars based on SSPP-P8. The solid line indicates the literature value, while the dashed line is the average value reported by SSPP-P8 for a given cluster. Compared with the SSPP-7 plot shown in Figure A3, note that the slight offsets between the overall means of SSPP-P8 and the literature values for M15, M2, and M67 are much smaller.

for the metallicity after subtracting the errors in quadrature. Similarly, for gravity estimates, the error of the HET high-resolution spectra is 0.129 dex; accepting 0.24 dex as the SSPP-P8 error, and taking a quadratic subtraction of the two errors, including the 0.1 dex offset in SSPP-P8 as shown in the second panel of Figure A2, we obtain an expected error of 0.225 dex. Considering that the SDSS/SEGUE spectra are rather low resolution, these error estimates are remarkably good. They would be even lower if we had a more uniform analysis of the high-resolution spectra available, a process that is now underway.

There are also various minor changes made on the SSPP. These changes help identify peculiar spectra and those with ill-measured parameters.

The calibration effort to improve parameter estimation of the SSPP will continue, focusing in particular on super metal-rich dwarfs, very low-gravity stars, low-metallicity stars, and cooler stars.

REFERENCES

Abazajian, K., et al. 2003, AJ, 126, 2081
Abazajian, K., et al. 2004, AJ, 128, 502
Abazajian, K., et al. 2005, AJ, 129, 1755
Abazajian, K., et al. 2009, ApJS, 182, 543
Adelman-McCarthy, J. K., et al. 2006, ApJS, 162, 38
Adelman-McCarthy, J. K., et al. 2007, ApJS, 172, 634
Adelman-McCarthy, J. K., et al. 2008, ApJS, 175, 297
Allende Prieto, C., Beers, T. C., Wilhelm, R., Newberg, H. J., Rockosi, C. M., Yanny, B., & Lee, Y. S. 2006, ApJ, 636, 804
Allende Prieto, C., et al. 2008, AJ, 136, 2070
An, D., et al. 2008, ApJS, 179, 326
An, D., et al. 2009, ApJ, 700, 523
Anthony-Twarog, B. J., Tanner, D., Cracraft, M., & Twarog, B. A. 2006, AJ, 131, 461
Arellano Ferro, A., Giridhar, S., & Bramich, D. M. 2010, MNRAS, 402, 226
Barrado Y Navascués, D., Deliyannis, C. P., & Stauffer, J. R. 2001, ApJ, 549, 452
Beers, T. C., Rossi, S., Norris, J. E., Ryan, S. G., & Shefler, T. 1999, AJ, 117, 981
Boesgaard, A. M., Jensen, E. E. C., & Deliyannis, C. P. 2009, AJ, 137, 4949
Boesgaard, A. M., King, J. R., Cody, A. M., Stephens, A., & Deliyannis, C. P. 2005, ApJ, 629, 832
Carraro, G., Girardi, L., & Marigo, P. 2002, MNRAS, 332, 705
Carretta, E., et al. 2009, A&A, 508, 695
Cavallo, R. M., & Nagar, N. M. 2000, AJ, 120, 1364
Cenarro, A. J., Cardiel, N., Gorgas, J., Peletier, R. F., Vazdekis, A., & Prada, F. 2001a, MNRAS, 326, 959
Cenarro, A. J., Gorgas, J., Cardiel, N., Pedraz, S., Peletier, R. F., & Vazdekis, A. 2001b, MNRAS, 326, 981
Cohen, J. G., Behr, B. B., & Briley, M. M. 2001, AJ, 122, 1420
Cohen, J. G., & Meléndez, J. 2005, AJ, 129, 303
Dékány, I., & Kovács, G. 2009, A&A, 507, 803
Dias, W. S., Alessi, B. S., Moitinho, A., & Lepine, J. R. D. 2002, A&A, 389, 871
Drukier, G. A., et al. 2007, AJ, 133, 1041
Fukugita, M., Ichikawa, T., Gunn, J. E., Doi, M., Shimasaku, K., & Schneider, D. P. 1996, AJ, 111, 1748
Geller, A. M., Mathieu, R. D., Braden, E. K., Meibom, S., Platais, I., & Kolan, C. J. 2010, AJ, 139, 1383
Gratton, R., Bragaglia, A., Carretta, E., & Tosi, M. 2006, AJ, 642, 462
Grundahl, F., Stetson, P. B., & Anderson, M. I. 2002, A&A, 395, 481
Gunn, J. E., et al. 1998, AJ, 116, 3040
Gunn, J. E., et al. 2006, AJ, 131, 2332
Harris, W. E. 1996, AJ, 112, 1487
Jacobson, H. R., Friel, E. D., & Pilochowski, C. A. 2009, AJ, 137, 4753
Kalirai, J. S., Fahlman, G. G., Richer, H. B., & Ventura, P. 2003, AJ, 126, 1402
King, J. R., et al. 1998, AJ, 115, 666
Kraft, R. P., & Ivans, I. I. 2003, PASP, 115, 143
Ivezić, Z., et al. 2008, ApJ, 684, 287
Lai, David K., et al. 2009, ApJ, 697, 63
Lane, R. R., et al. 2009, MNRAS, 400, 917
Lane, R. R., et al. 2010, MNRAS, 401, 2521
Lee, Y. S., et al. 2008a, AJ, 136, 2022 (Paper I)
Lee, Y. S., et al. 2008b, AJ, 136, 2050 (Paper II)
Lupton, R., et al. 2001, in ASP Conf. Ser. 238, Astronomical Data Analysis Software and Systems X, ed. F. R. Harnden, Jr., F. A. Primini, & H. E. Payne (San Francisco, CA: ASP), 269
Morrison, H. L., Norris, J., & Mateo, M., et al. 2003, AJ, 125, 2502
Origlia, L., Valenti, E., Rich, R. M., & Ferraro, F. R. 2006, ApJ, 646, 499
Pier, J. R., Munn, J. A., Hindsley, R. B., Hennessy, G. S., Kent, S. M., Lupton, R. H., & Ivezić, Z. 2003, AJ, 125, 1559
Pilachowski, C. A., Bothun, G. D., Olszewski, E. W., & Odell, A. 1983, ApJ, 273, 187
Ramírez, S. V., Cohen, J. G., Buss, J., & Briley, M. M. 2001, AJ, 122, 1429
Randich, S., et al. 2006, A&A, 450, 557
Re Fiorentin, P., Bailer-Jones, C. A. L., & Lee, Y. S., et al. 2007, A&A, 467, 1373
Schlegel, D. J., Finkbeiner, D. P., & Davis, M. 1998, ApJ, 500, 525
Scott, J. E., Friel, E. D., & Janes, K. A. 1995, AJ, 109, 1706
Sneden, C., et al. 2004, AJ, 127, 2162
Stetson, P. B. 1987, PASP, 99, 191
Stetson, P. B. 1994, PASP, 106, 250
Stoughton, C., et al. 2002, AJ, 123, 485
Twarog, B. A., Ashman, K. M., & Anthony-Twarog, B. J. 1997, AJ, 114, 2556
Wilhelm, R., Beers, T. C., & Grays, G. W. 1999, AJ, 117, 2308
Worthey, G., & Jowett, K. J. 2003, PASP, 115, 96
Yanny, B., et al. 2009, AJ, 137, 4377